ENGINEERING MULTI-ELECTRON INTERACTIONS FOR QUANTUM LOGIC IN SILICON

A Dissertation

Submitted to the Faculty

of

Purdue University

by

Archana Tankasala

In Partial Fulfillment of the

Requirements for the Degree

of

Doctor of Philosophy

August 2017

Purdue University

West Lafayette, Indiana

THE PURDUE UNIVERSITY GRADUATE SCHOOL
STATEMENT OF DISSERTATION APPROVAL

Dr. Gerhard Klimeck, Chair

School of Electrical and Computer Engineering

Dr. Rajib Rahman, Co-Chair

School of Electrical and Computer Engineering

Dr. Sven Rogge

School of Physics, University of New South Wales, Australia

Dr. Supriyo Datta

School of Electrical and Computer Engineering

Dr. Michael J Manfra

School of Electrical and Computer Engineering

Approved by:

Dr. Venkataramanan Balakrishnan

Head of the School Graduate Program

Dedicated To

my darling grandmother, my beloved parents, my godfather and my little sister

ACKNOWLEDGMENTS

I express my sincere gratitude to my advisor, Prof. Gerhard Klimeck, who has provided me with both academic and financial support during my PhD. I would like to thank him for the wonderful opportunity to be a part of nanoHUB and NCN at Purdue and for access to excellent computing resources. I am extremely grateful to Prof. Rajib Rahman, for being an awesome mentor. I am thankful for his patience during my learning phase and his support and encouragement even during the unproductive phases of my PhD. I would like to thank both Gerhard and Rajib for trusting me with such wonderful projects, knowing my lack of expertise in physics and nano-electronics.

I feel fortunate to have had the opportunity to work with one of the best experimental research groups in quantum computing. Prof. Sven Rogge and his team at UNSW; Dr, Juanita Bocquel, Dr. Joseph Salfi and Dr. Benoit Voisin have been a great source of knowledge and my exposure to the experiments. I appreciate the collaboration with Prof. Lloyd Hollenberg and Dr. Muhammad Usman. I enjoyed interacting with them and learnt a lot from the weekly meetings. Special thanks to Prof. Supriyo Datta and Prof. Michael Manfra for serving on my committee. I appreciate their time, effort and support. I am also thankful to the quantum computing team Yuling Hsueh, Yu Wang, Rifat Ferdous and Harshad Sahasrabudhe for useful discussions on research projects.

"It's the friends we meet along the way that help us appreciate the journey". I am grateful to all my friends for their part in my journey: my friend, philosopher and guru, Hesameddin Ilatikhameneh; my dearest sister-friend, Fan Chen; my friend and teacher, Tarek Ameen; my close friends ChinYi Chen and Daniel Valencia; my friends YuanChen Chu, Kuang-Chung Wang, Kai Miao and Amanda Blagg; for making the fun times better and the tough times easier. I am thankful for the useful suggestions and guidance from Yui-Hong Matthias Tan and Mehdi Salmani Jelodar.

Most of all, I owe deepest gratitude to my family: my beloved grandmother, Janaki Goturu; wonderful parents, Narasinga Rao Tankasala, Padmavati Tankasala; my godfather, Rama Rao Goturu and my best friend - my little sister, Harika Tankasala; for being a constant source of strength and support.

TABLE OF CONTENTS

Page

LIST OF TABLES

LIST OF FIGURES

Figure Page

Figure Page

Figure Page

Figure Page

Figure Page

Figure Page

ABSTRACT

Tankasala, Archana Ph.D., Purdue University, August 2017. Engineering multi-electron interactions for quantum logic in silicon. Major Professor: Gerhard Klimeck.

Solid-state platforms are promising candidates for future quantum computers. Recent advances in solid-state nano-electronics have enabled precise control of individual atoms at atomic scales and manipulation of single qubits. Demonstration of high-fidelity two-qubit operations is being actively pursued and is currently the most sought after problem in the field of semiconductor quantum computing. A precise control of a two-qubit gate typically requires an in-depth understanding of the exchange of information between the electrons, which is complicated by the complex many-body quantum phenomena like correlation and entanglement. Accurate modeling of electron interactions is therefore of crucial importance in the effort towards scalable multi-qubit devices in the solid state.

Atomistic Configuration Interaction (ACI), a portable, efficient and scalable computational tool for modeling electron-electron interactions in multi-electron quantum devices is implemented in the Nano-Electronic MOdeling (NEMO) software suite. The tool is validated against experimental data, in collaboration with the Centre for Quantum Computing and Communication Technology. Two-electron spectra and charge clouds are imaged at CQCCT and mapped to ACI simulation results to better understand electronic interactions on an atomic-scale in single donor atoms and coupled donor pairs. Furthermore, ACI is employed to investigate novel qubit architectures. Two-spin singlet-triplet and three-spin exchange-only qubits based on dopant atoms in silicon, enabling an all-electrical qubit control, are proposed and two-axis rotations towards electrically-controlled single qubit logic gates are demonstrated theoretically using ACI.

1. INTRODUCTION

Scientific computation enables computer experiments on physical systems ranging from predictive simulations of climate, sub-atomic particle behavior and engineering to data mining and security. An accurate modeling of realistic systems demands high-speed processing of a huge amount of data. To meet these requirements, an exponential improvement in the performance of a single processor has been aggressively achieved over the last few decades, by scaling down the dimensions of a single transistor to increase the transistor density per processor [1, 2]. But this continued increase in performance is expected to saturate due to fundamental limitations imposed by quantum mechanics in scaling down the transistor dimensions further [3]. Alternately, several thousands of these processors are used in parallel to handle large volumes of data for high-performance computing with the modern supercomputer. It is however estimated that exaFLOP speeds require significant changes to the current supercomputing hardware architectures but zetaFLOP computing is nearly impossible to achieve [4]. Among the several alternatives being actively explored, quantum computing presents a promising future towards an exponential increase in the computational capabilities, by exploiting the fundamental quantum effects like superposition and entanglement, that have been limiting the performance of the modern transistors [5].

A quantum computer exponentially outperforms its classical counterpart for a certain class of algorithms [6–8]. The advantage comes from inherent parallelism of qubit operations. A single classical bit can only carry a single piece of information, transistor ON or OFF. A system of n-classical bits can exist in 2^n states but at a certain point in time, can exist in only one of these possible states. So multiple classical bits can still only hold a single piece of information. However, a single quantum bit can exist in a linear superposition of the states of a two-level system, like polarization

of light or electron or nuclear spin. The quantum bit, or *qubit*, in such a superposed state is represented as $|\Psi\rangle = a\,|\uparrow\rangle + b\,|\downarrow\rangle$ where $|\uparrow\rangle$ and $|\downarrow\rangle$ are the basis states of the two-level qubit system. So a single qubit can hold two pieces of information at the same time and by extension, n coupled qubits can simultaneously hold 2^n pieces of information. Moreover, an operator on n classical bits acts only on a single state of the n-bit system but an operator on an n quantum bit system can act on all the 2^n states in parallel. This inherent parallelism of qubit operations makes a quantum computer exponentially faster than a classical computer. A 30-qubit quantum computer is estimated to be more powerful than a modern day supercomputer [9,10].

1.1 Electron Spin Qubits

A single electron spin is a natural two-level system for a qubit. In the presence of a static magnetic field B, the electron spin has two states, its spin oriented in the direction of magnetic field $|\uparrow\rangle$ and opposite to the direction of magnetic field $|\downarrow\rangle$. The two states are separated by Zeeman splitting $E_Z = g\mu_B B$ in energy, where g is the electron g-factor and μ_B the Bohr magneton. Electron can exist in a superposition of $|\uparrow\rangle$ and $|\downarrow\rangle$ states which is fundamental to a qubit operation.

A single qubit operation involves qubit initialization, manipulation and measurement, as shown in Fig. 1.1. Qubits must be initialized to a well-defined state on the Bloch sphere with a high fidelity. Qubit manipulation involves changing qubit state from $|\Psi\rangle$ to $|\Phi\rangle$ represented as distinct points on the Bloch sphere. Such manipulations require qubit state rotations about two axes on the sphere, typically X and Z. For a single electron spin qubit, an oscillating magnetic field couples the two spin states and drives the transitions between the states [11, 12]. After successful manipulation, the qubit must be read-out with a high fidelity to measure its state [13, 14]. An ensemble of repeated measurements on the state project the qubit state to one of the basis states with a certain probability.

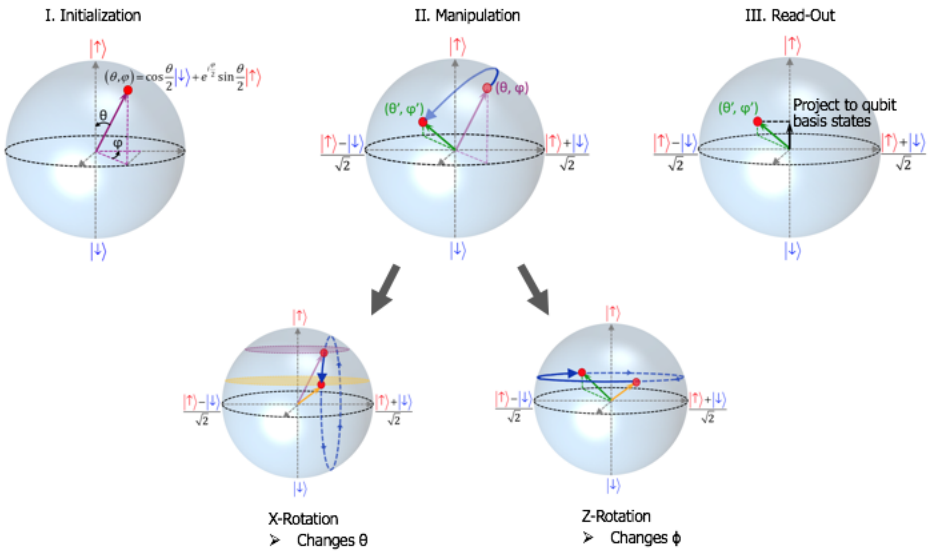

Fig. 1.1. Bloch sphere representation of a single qubit operation. Qubit basis states on the Z-axis. (a) Initialization to any point (θ,ϕ) on Bloch sphere. (b) Manipulation. Two-axis rotations to manipulate the qubit state. (c) Read-out. Project the qubit states onto the basis states.

For a coherent control of a single electron spin, the electron must be confined in all three dimensions. Typically, this has been achieved in semiconductor based devices by electrostatically confining the electrons to gate-defined quantum dots or by Coulombically confining the electrons to single dopant atoms in silicon. As shown in Fig. 1.2(a), in GaAs-AlGaAs heterostructures, the electrons are confined to quantum dots defined electrostatically by the gates positioned on the surface of a two-dimensional electron gas, 2DEG formed at the GaAs-AlGaAs interface [12,15,16]. The potential of these dots is tuned by a different top gate, called the plunger gate. Si-MOS or Si-SiGe structures can also be used to confine an electron electrostatically instead of GaAs-AlGaAs [17, 18]. Electrons can alternately be confined to a Coulombic donor atom potential in silicon instead of an electrostatic confinement from the top gates, as in Fig. 1.2(b) [11,19]. Donors offer a natural confinement to the electron and the potentials of these dopant atoms are consistent making the donor-based qubits promising

towards scalable quantum computing. Recent experiments demonstrate deterministic placement of the dopant atoms using STM lithography techniques which provides a good control on the position of the Coulomb confined dot [20]. Donor bound electron spins have been shown to have exceptionally long coherence times exceeding several seconds at cryogenic temperatures making the spins of these electrons attractive and promising for quantum information processing [21]. Moreover, both of these semiconductor based electron spin qubits take advantage of current fabrication technologies of the electronics industry and are hence more appealing towards quantum computing applications.

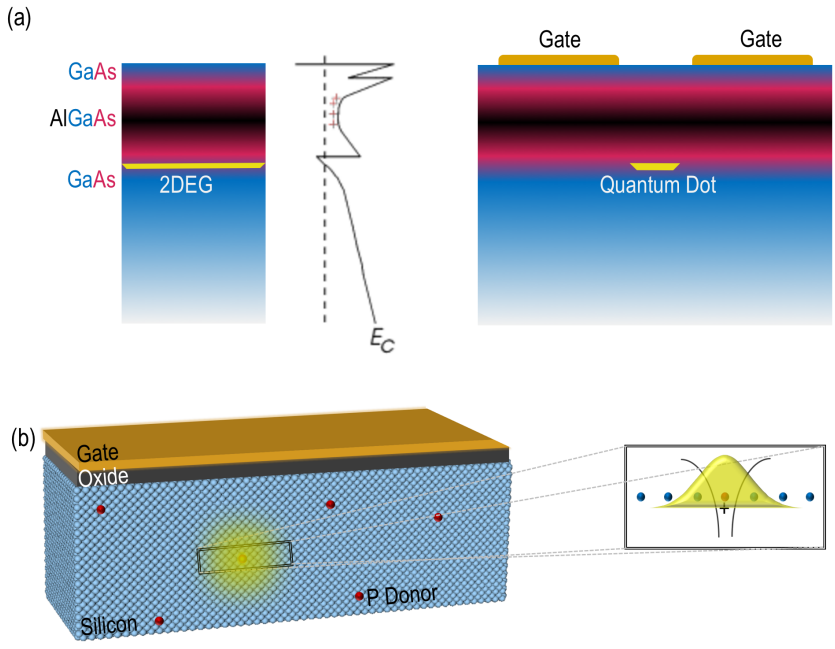

Fig. 1.2. 3-dimensional electron confinement. (a) Electrostatic gate-defined quantum dots. 2-dimensional electron gas (2DEG) at the GaAs-AlGaAs interface of the heterostructure, as seen from the band diagram (E_C in solid line) and Fermi level (in dashed line). Top depletion gates deplete the electrons under them and define the quantum dot in the 2DEG. (b) Dopants. Phosphorous dopants in a silicion MOS structure. Additional nuclear charge of the donor in a silicon background leads to Hydrogenic Coulombic potential and energy levels that confine an electron 3-dimensionally.

Coherent control of a single electron spin qubit has been successfully demonstrated in electrons confined 3-dimensionally to electrostatic gate-defined quantum dots and to single dopant atoms in silicon. Towards the realization of a scalable quantum computing architecture, the next big challenge is the two-qubit gate operation. For electron spin qubits, two-qubit operations rely on the electron-electron interactions, that can be tuned electrically with gate biases. For a precise gate control of a two-qubit operation, an accurate estimate of electron-electron interactions, taking into account the atomistic details of realistic devices is, therefore, critical.

In this work, atomistic tight-binding is used to model electron wavefunctions in realistic, multi-million-atom devices, considering the atomistic effects of interfaces, defects and complex geometries. For few-electron systems, the energy spectra and the multi-electron spin configurations, including the electron-electron interactions, are obtained from Atomistic Configuration Interaction, ACI. ACI method is introduced in chapter 2. The methodology and implementation of ACI in Nano-Electronic MOdeling, NEMO software suite [22, 23] are discussed and some of the computational challenges with respect to performance and memory are addressed. Chapter 3 presents experimental validation of the ACI simulation tool for (1) a single negative donor in bulk silicon, (2) a single negative donor in silicon close to the surface probed by scanning tunneling microscope, STM, (3) a neutral donor pair in silicon, and (4) multi-electron GaAs quantum dot. A successful validation allows the application of ACI method to gain a deeper understanding of the physics of (1) a single negative donor in silicon located close to the surface, and (2) neutral donor pairs in silicon, discussed in chapter 4. ACI is employed to explore novel qubit architectures; multi-electron qubits based on dopants in silicon, detailed in chapter 5. Lastly, chapter 6 summarizes the ACI method, the results and discusses possible future work.

2. METHODOLOGY

Semiconductor based electron spin qubits rely on the wavefunction of electrons for their operation; its spatial spread in the real and reciprocal space and its spin. An electron wavefunction in multi-valley host materials like silicon, therefore, has three degrees of freedom; orbital, valley and spin. Electrons can be confined in all three dimensions to electrostatically defined quantum dots or Coulombic donor potentials, as described in the previous chapter. In dots, complex gate geometries and atomic scale inhomogenities in the confining interface can significantly influence the orbital, valley and spin properties of the electron wavefunction [17, 18, 24]. For donors, in the absence of spin-orbit interaction, the confining Coulombic potential varies sharply over atomic distances which couples the orbital and valley states of the bound electron wavefunction [25]. It is therefore critical, in both electrostatic quantum dot and dopant systems, to capture the atomistic details of the system in determining the exact electron wavefunction. Moreover, the crystal symmetries of the host material and its bandstructure also effect the valley states. Semi-emperical atomistic tight-binding (TB) has been shown to not only capture the subtle effects of these atomistic defects [26, 26] but also explain several high-profile experiments like the single-atom transistor and world's thinnest nanowire [27, 28].

Two qubit gate operations in electron spin qubits rely on the interactions between electron spins. Even single qubit operations in multi-spin qubits based on electrostatic quantum dots, like singlet-triplet qubit, exchange-only, resonant exchange qubit rely on interactions between electron spins [29, 29–33]. The gate rotations are extremely sensitive to the electron-electron interactions and it is, therefore, critical to obtain

a precise estimate. Full Configuration Interaction (FCI) is an exact method to determine electron interactions; it captures the Coulomb repulsion between electrons, exchange interactions of electron spins and electron correlation [34].

In this work, realistic few-electron devices in semiconductors are modeled using Atomistic Configuration Interaction (ACI), an atomistic many-body approach based on atomistic tight-binding and full configuration interaction. Single electron wavefunctions, both spatial and spin resolved on an atomic scale, in a multi-million atom domain are obtained from atomistic tight-binding method in NEMO3D and NEMO5 [22, 23]. These wavefunctions are used to construct an orthonormal basis of anti-symmetrized few-electron wavefunctions, called Slater determinants. Many-body Schrödinger equation is solved in the Slater determinant basis to obtain many-electron eigenenergies and eigenfunctions using FCI. However, as will be shown later, ACI is computationally demanding, especially for large simulation domains and strongly confined electrons. Two different approaches are implemented to improve the performance of ACI and obtain faster simulation results. This chapter details the methodology and implementation of the ACI towards its use in modeling few-electron semiconductor devices.

2.1 Atomistic Tight-Binding

In atomistic tight-binding approach, the system is modeled as lattice of atoms. Atomic orbitals $sp^3d^5s^\star$ localized on each of these atoms form the 10-band basis for single-electron wavefunctions [35, 36]. The parameters of the semi-empirical model are fit to match the features of the experimental band structure or $ab-initio$ methods like Density Functional Theory (DFT). 20-band basis, including the spin-orbit coupling parameters, are used in the presence of spin-orbit interactions or external magnetic fields. Atomistic effects of interfaces, complex geometries, defects and multi-valley coupling are accurately determined with this approach [37–39]. Large system domains, involving millions of atoms, model a realistic electron confinement

and ensure the excited wavefunctions of the electron are not affected by the artificial domain boundaries. In the nearest-neighbor tight-binding aproximation, the Hamiltonian is sparse and diagonalized using Block Lanczos eigensolver, that can resolve degeneracies and closely spaced higher energy states [40]. While the general approach is the same, an external potential from the gates of the electrostatic dot or the donor nucleus is added to the diagonal elements of the tight-binding Hamiltonian. The following sections discuss the details of modeling, including the confining potential in this tight-binding approach for electrostatic quantum dot and dopant systems, to obtain single-electron wavefunctions.

2.1.1 Electrostatically Defined Quantum Dots

An electron is confined 3-dimensionally in electrostatic dots by an electric field perpendicular to the interface and by lateral fields from the accumulation or depletion top gates. The corresponding potential can be approximated to be linear (due to constant field) perpendicular to the interface and parabolic laterally [41]; or can be obtained from TCAD simulation software like COMSOL Multiphysics; or from self-consistently solving Poisson with Schrödinger (semi-classically with an effective mass approach) in NEMO5 [42], listed in the order of increasing accuracy.

2.1.2 Dopants

A phosphorous donor in a silicon lattice has a single additional positive charge at its nucleus. The resulting confinement from this donor is hydrogenic and therefore, is modeled as a Coulomb potential. To ensure convergence of this singular potential and consider the effect of dielectric screening, the potential at donor core, close to the singularity, is approximated with empirically determined central cell correction, i.e. the Coulomb potential is cut-off at $r = r_c$, the critical radius. This method is shown to correctly determine the energy spectrum of a single donor (P, As) in silicon [37,38].

2.2 Full Configuration Interaction

Given single-electron wavefunctions $\psi_a(\vec{r})$ and $\psi_b(\vec{r})$, where $\vec{r}$ is 4-dimensional vector of spatial and spin coordinates (x, y, z, ω) of the electron, the simplest two-electron wavefunction that can be constructed is the product of the two single-electron wavefunctions, the Hartree product:

$$\Psi(\vec{r}_1, \vec{r}_2) = \psi_a(\vec{r}_1)\psi_b(\vec{r}_2) \tag{2.1}$$

where $\vec{r}_1$ and $\vec{r}_2$ are the coordinates of the two electrons. However, such a wavefunction distinguishes between the two electrons and it can be claimed that electron at $\vec{r}_1$ occupies single-electron state ψ_a and electron at $\vec{r}_2$ the state ψ_b. Indistinguishable Fermionic electrons must have an anti-symmetric wavefunction, which means that the electrons should be indistinguishable from the wavefunction and exchanging the coordinates of the two electrons should induce a negative sign on the two-electron wavefunction. This anti-symmetry is a manifestation of Pauli's exclusion principle which states that electrons with identical spins cannot occupy the same orbital state. Equation 2.1 can therefore be anti-symmetrized to obtain Hartre-Fock wavefunction:

$$\Psi(\vec{r}_1, \vec{r}_2) = \frac{1}{\sqrt{2}} \{\psi_a(\vec{r}_1)\psi_b(\vec{r}_2) - \psi_b(\vec{r}_1)\psi_a(\vec{r}_2)\} \tag{2.2}$$

Hartree product, equation 2.1, is an independent electron approximation; it does not allow for interactions of electron spins. The electrons only feel the averaged field due to the other electrons. It captures the Coulomb energy J which is the classical electrostatic repulsion between the charge clouds of electrons. Hartree-Fock wavefunction, equation 2.2, is anti-symmetrized with respect to interchange of electron coordinates thus making the electrons indistinguishable, unlike the Hartree product. It can also be verified that there is a finite probability of finding both electrons at the same spatial coordinate in the Hartree product approximation, equation 2.1). In the Hartree-Fock approximation, equation 2.2, the probability of finding electrons with parallel spins at the same spatial coordinate is zero and therefore, it can correlate parallel spin electrons and hence also capture the exchange interaction K. However,

electrons with anti-parallel spins still remain uncorrelated, since even the Hartree-Fock wavefunction, equation 2.2, misses the interactions of electrons with opposite spins. Written in a matrix form, equation 2.2

$$\Psi(\vec{r}_1, \vec{r}_2) = \frac{1}{\sqrt{2}} \begin{bmatrix} \psi_a(\vec{r}_1) & \psi_a(\vec{r}_2) \\ \psi_b(\vec{r}_1) & \psi_b(\vec{r}_2) \end{bmatrix} \tag{2.3}$$

is called a Slater determinant $|a, b\rangle$ representation of states ψ_a and ψ_b.

A single Slater determinant represents only one of the possible configurations of the two-electron state, the ground state. A more exact method should ideally include all possible configurations, including the excited states of the system. For example, from a set of single-electron wavefunctions $\{\psi_a(\vec{r}), \psi_b(\vec{r}), \psi_c(\vec{r}), ...\psi_r(\vec{r}), \psi_s(\vec{r}), ...\psi_n(\vec{r})\}$, Slater determinants of different configurations can be constructed. $|\Psi_0\rangle = |ab\rangle$ is the ground state, which is the Hartree-Fock wavefunction. However, singly-excited Slater determinant configurations like $|\Psi_a^r\rangle$ can be constructed from promoting an electron in state ψ_a to excited state ψ_r or doubly-excited configurations $|\Psi_{ab}^{rs}\rangle$ from promoting both electrons in states ψ_a and ψ_b to states ψ_r and ψ_s and so on. These Slater determinants corresponding to different electron configurations form a complete orthonormal basis set and can be employed in defining any arbitrary two-electron state as a superposition of these basis states.

Full Configuration Interaction, FCI [34] represents a two-electron wavefunction as a linear superposition of all possible Slater determinant configurations as

$$\Psi(\vec{r}_1, \vec{r}_2) = C_0 |\Psi_0\rangle + \sum_{a,r} C_a^r |\Psi_a^r\rangle + \sum_{ab,rs} C_{ab}^{rs} |\Psi_{ab}^{rs}\rangle \tag{2.4}$$

where $|\Psi_0\rangle$ is the ground state Slater determinant and $|\Psi_a^r\rangle$ and $|\Psi_{ab}^{rs}\rangle$ are the singly and doubly excited Slater determinants, respectively. Two-electron Schrödinger equation can be diagonalized in this Slater determinant basis to obtain the exact two-electron eigenenergies and eigenfunctions. This section describes the FCI method for two electron systems for simplicity but the method can easily be extended to few-electron systems.

2.3 Atomistic Configuration Interaction

Modeling few-electron semiconductor devices used for quantum computing applications, especially as electron or nuclear spin qubits, require an accurate capture of the atomistic details of the system and electron-electron interactions. Atomistic Configuration Interaction, ACI solves for the few-electron states of the system using configuration interaction method in the Slater determinant basis constructed from a set of orthonormal single-electron states obtained from semi-emperical atomistic tight-binding. The method can, therefore, capture both the atomistic effects and the electron interactions precisely. This section describes, in detail, the ACI method and its implementation into the NEMO software suite.

Semi-emperical atomistic tight-binding in NEMO, both NEMO3D and NEMO5 [22,23], solves for single-electron Schrödinger equation in the basis of localized $sp^3d^5s^\star$ atomic orbitals i.e it constructs the Hamiltonian of the system for a single electron. The Hamiltonian is diagonalized using Block Lanczos eigensolver that can resolve the eigenstate degeneracies. Resulting eigenvalues are the single-electron energy levels and the corresponding eigenfunctions are the single-electron wavefunctions. For both electrostatic dot and dopant systems, the single-electron wavefunctions are spread over millions of atoms in the simulation domain and each of them is resolved over atoms, orbitals and spins.

Several of these single-electron states (ranging from 10 in large electrostatic quantum dots to 150 in highly confined donors) are required in constructing the Slater determinant basis for CI. Using n single-electron states for an e-electron system, the number of Slater determinants are ${}^nC_e$, which is the size of the few-electron CI Hamiltonian defined in the Slater determinant basis. Within Born-Oppenheimer approximation, the electronic Hamiltonian of an n-electron system is given by:

$$\mathcal{H} = -\sum_{i=1}^{n} \frac{1}{2}\nabla_i^2 - \sum_{i=1}^{n}\sum_{A=1}^{N} \frac{Z_A}{r_{iA}} + \sum_{i=1}^{n}\sum_{j>i}^{n} \frac{1}{r_{ij}} \tag{2.5}$$

The first term in the equation is the kinetic energy of electrons, second term corresponds to the the interaction energy between electrons and nuclei and the third term is

the interaction among electrons themselves. In the basis of possible n-electron Slater determinants $|a\rangle = |\psi_i\psi_j...\rangle$ and $|b\rangle = |\psi_k\psi_l...\rangle$, the Hamiltonian element $\mathcal{H}(a,b)$ is $\langle\psi_i\psi_j...|\,\mathcal{H}\,|\psi_k\psi_l...\rangle$ where the ψs are the single-electron states of the system, in the basis of localized atomic orbitals at each atom, as obtained from atomistic TB method.

The Hamiltonian, split into single-electron and two-electron operators, acting on the Slater determinants is $\langle\psi_i\psi_j|\,\mathcal{O}_1 + \mathcal{O}_2\,|\psi_k\psi_l\rangle$ where $\mathcal{O}_1 = -\sum_{i=1}^{n}\frac{1}{2}\nabla_i^2 - \sum_{i=1}^{n}\sum_{A=1}^{N}\frac{Z_A}{r_{iA}}$ and $\mathcal{O}_2 = \sum_{i=1}^{n}\sum_{j>i}^{n}\frac{1}{r_{ij}}$. One-electron terms are integrals over coordinates of a single electron which can be reduced to a simple sum of energies of single-electron states involved in Slater configurations. The off-diagonal elements are zeros due to the orthonormality of the single-electron TB wavefunctions. The diagonal elements are simply the eigenenergies obtained from TB simulations.

However, two-electron terms need an evaluation of Coulomb J and exchange K integrals,

$$J = \langle ij|\,kl\rangle = \iint_V \psi_i^*(\vec{r}_1)\psi_j^*(\vec{r}_2)\frac{1}{|\vec{r}_1 - \vec{r}_2|}\psi_k(\vec{r}_1)\psi_l(\vec{r}_2)\,\mathrm{d}\vec{r}_1\mathrm{d}\vec{r}_2 \tag{2.6}$$

$$K = \langle ij|\,lk\rangle = \iint_V \psi_i^*(\vec{r}_1)\psi_j^*(\vec{r}_2)\frac{1}{|\vec{r}_1 - \vec{r}_2|}\psi_l(\vec{r}_1)\psi_k(\vec{r}_2)\,\mathrm{d}\vec{r}_1\mathrm{d}\vec{r}_2 \tag{2.7}$$

between every combination of indices i, j, k and l ranging from 1 to n. With the single-electron wavefunctions expanded in the basis of localized atomic orbitals, the integrals are singular when both electrons are localized at the same atom, $\vec{r}_1 = \vec{r}_2$. The singularity is treated with an emperical parameter corresponding to a minimum separation between two electrons. Each of $J = \langle ij|\,kl\rangle$ and $K = \langle ij|\,lk\rangle$ is a double integral over the 3-dimensional coordinates and therefore, 6-dimensional to be evaluated over the entire region of simulation domain V. It is obvious that the evaluation of these integrals towards the construction of ACI Hamiltonian is computationally more expensive than the diagonalization of ACI Hamiltonian to obtain few-electron energies and wavefunctions. The diagonalization of the Hamiltonian is optimized using both LAPACK and FEAST eigen solvers. FEAST is very fast in evaluating the eigenfunctions since it only solves for the eigenstates in a specified range [43]. This

range is obtained from LAPACK, solved only for eigenvalues which is fast [44], and fed to FEAST. Solutions to the ACI Hamiltonian give the energy levels of the few-electron states of the system and the contributions from each Slater configurations to these states. The correlations are evident from these eigenfunctions of the ACI Hamiltonian. It must be noted that the solution from FCI is exact as long as the basis set is complete. In practise, however, a truncated basis set is used in ACI due to computational limitations.

Screening of electron-electron interactions

An important feature of ACI implemented in NEMO is to capture the effect of electrostatics of the system on electron-electron interactions. Presence of interfaces and dielectric mismatches renormalize and screen the electron-electron interactions. This effect is captured in ACI using the method of images charges [45].

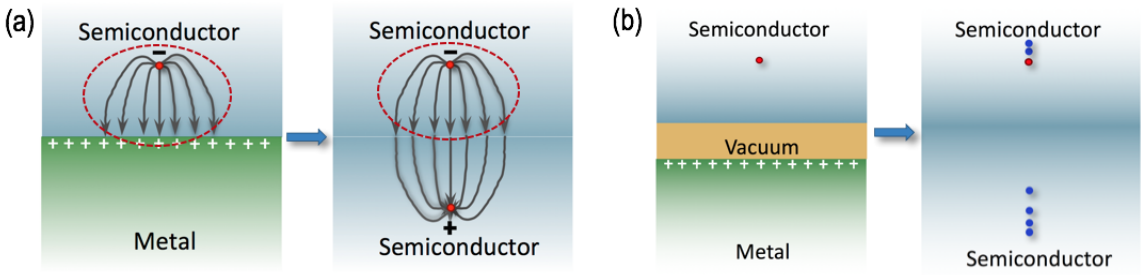

Fig. 2.1. Approximating the potential profile in the semiconductor region using the method of image charges. (a) Metal-Semiconductor interface requires single image charge of opposite polarity. (b) Metal-Insulator-Semiconductor interface requires multiple reflections of the image charges.

The electric field due to a point charge is modified (from being radial and spherically symmetric) due to a metal-semiconductor interface as shown in Fig. 2.1(a). The field is approximated by replacing the metal region by a point charge of opposite polarity, called the image charge. As seen in Fig. 2.1(a), the field within the region of

interest, highlighted in red, is similar with a metal interface or with an image charge, and they generate the same potential profile in the semiconductor region. For more complex interfaces, it is not sufficient to include just one image charge as shown in Fig. 2.1(b) but several reflections of the image charges across different interfaces for a fairly approximate description of the potential profile in the semiconductor region.

To determine the number of image charges that are required to accurately capture the potential profile in the semiconductor region, the structure shown in Fig. 2.2(a) is simulated in COMSOL for different insulator (vacuum in this case) thickesses that are typical in STM experiments. A point charge is placed close to the semiconductor-vacuum interface, 3nm deep and the metallic gate (the tip in an STM set-up) is assumed to be grounded. Fig. 2.2(b) shows that the analytical image charge method matches the COMSOL potentials only when up to 10 image charges are included in the analytical method for 0.5nm vacuum thickness, dimension of interest for STM experiments.

ACI uses the same technique of image charges to capture the effect of electrostatics of the interfaces on electron-electron interactions. Here, the Coulomb and exchange interactions of the electron are evaluated, not only between two electrons, but also between an electron and several reflections of images of the other electron. This considerably increases the computational burden in evaluation of each matrix element of ACI Hamiltonian. However, the inclusion of these image charges, to capture the screening of electron interactions due to interfaces, is necessary for an accurate quantitative evaluation of the few-electron states of a quantum dot or dopant.

2.3.1 Addresssing the computational challenges in ACI

For a simulation domain of 2 million atoms, which is typical for realistic quantum computing devices, a single TB wavefunction, resolved over atoms, orbitals and spins, is a 40 million long vector of complex numbers. As will be shown later, highly confined systems need over 100 single-electron states in the basis to construct Slater

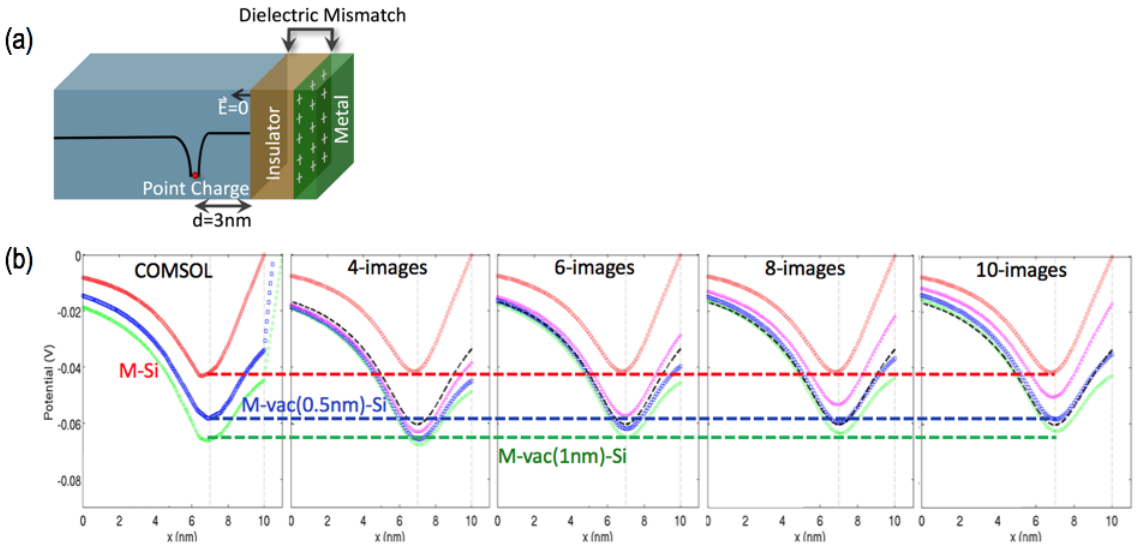

Fig. 2.2. Benchmarking the analytical method of image charges against COMSOL. (a) Metal-Insulator-Semiconductor structure with a point charge placed at d=3nm from the interface and the metal is grounded. (b) Potential profile in the semiconductor region of the structure for different insulator (vacuum) thicknesses. Up to 10 image charges are necessary for vacuum thicknesses larger than 0.5nm to obtain the same potential in the semiconductor as COMSOL.

determinants while weakly confined need about 10. For example, assuming 30 single-electron states in the basis, the input to CI is a 30 x 40 million matrix of complex doubles. Constructing the ACI Hamiltonian requires evaluating all possible integrals of the form $\langle ij|\,kl\rangle$ and $\langle ij|\,lk\rangle$, i.e. $2 *^{30} C_2$ double integrals over 2 million atoms. The computational burden in evaluating these integrals comes from the r^{-1} Coulomb kernel that includes square root and division floating point operations to be done 4 million times for each of the $2 *^{30} C_2$ integrals. The complexity of the computations is $O(N^2 n^e)$, where N, n and e are the number of atoms, single-electron basis wave-functions and electrons, respectively. This challenge in the computational complexity of ACI is addressed with the following approaches, (1) Simulation time, (2) Memory, and (3) Performance. These are discussed in detail in this section.

Simulation time

Numerical evaluation of the double integrals J and K from equations 2.6 and 2.7 can easily be parallelized over several cores using MPI for distribution of computational burden. To keep the overhead from MPI communications to a minimum and to increase scalability, the atoms are distributed among the cores rather than distributing the wavefunctions or Slater determinants.

The main metrics of an efficient parallelization of any algorithm are (1) the strong scaling which indicates that the simulation time must decrease with increasing number of cores, (2) the weak scaling which indicates the simulation time must remain unchanged when the problem size and the number of cores are both increased together, and (3) overhead from the I/O and communication that must be minimized. The computation is massively parallelized for large systems with many single-electron states in the basis. Fig. 2.3 shows the scaling curves for ACI are close to ideal. The code scales upto 3000 cores and has an overhead of less than 2% as seen from profiling tools like Intel's VTune.

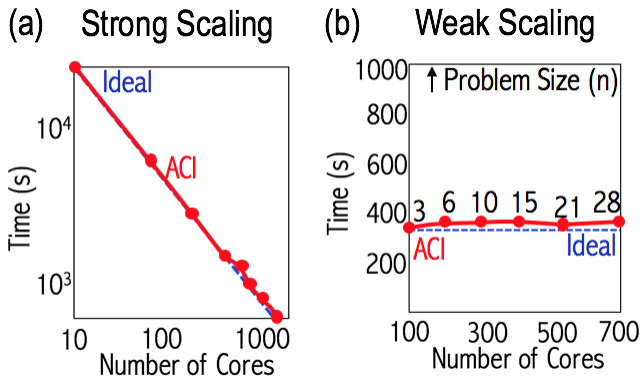

Fig. 2.3. Scaling of ACI. (a) Strong Scaling: increasing the number of cores decreases the simulation time. (b) Weak Scaling: increasing both the number of cores and the problem size (in this case, number of single-electron states in the basis) does not change the simulation time.

Memory

ACI simulations process a large volume of data. As mentioned in previous section, several single-electron wavefunctions resolved over atoms, orbitals and spins; wavefunction pair products like $\psi_i^*(\vec{r}_1)\psi_j(\vec{r}_1)$ that are saved in memory to reduce the number of repeated computations; Coulomb potential due to each of these pair products $\psi_i^*(\vec{r}_1)\psi_j(\vec{r}_1)\frac{1}{\vec{r}_1-\vec{r}_2}$; and so on. It is advantageous to make all this data available to each of the cores for read/write. This minimizes the communication overhead between the cores. Therefore, a shared memory model is used with OpenMP, where each node has a master core and the remaining cores are used as threads. The entire memory of the node is shared between the threads. The tasks for the threads are clearly assigned so there is minimum competition between the threads to read/write data to the shared memory. This approach has allowed the large-scale computations involving 2 million atoms and upto 60 single-electron states in the basis without running into memory problems.

Performance

While the above two approaches help greatly in reducing the computation time and memory requirements, it is also important to reduce the computational complexity of a simulation. A careful look at either of the J or K integrals from equations 2.6 and 2.7, by rearranging the terms, suggests that the integrals are equivalent (in an atomistic basis) to the summation as

$$\begin{aligned} J = \langle ij|\, kl\rangle &= \iint_V \psi_i^*(\vec{r}_1)\psi_k(\vec{r}_1)\frac{1}{|\vec{r}_1-\vec{r}_2|}\psi_j^*(\vec{r}_2)\psi_l(\vec{r}_2)\,\mathrm{d}\vec{r}_1\mathrm{d}\vec{r}_2 \\ &= \sum_{a=1}^{N}\sum_{b=1}^{N} q_{ik}(\vec{r}_a)\frac{1}{|\vec{r}_a-\vec{r}_b|}q_{jl}(\vec{r}_b) \end{aligned} \tag{2.8}$$

where $q_{ik}(\vec{r}_a) = \psi_i^*(\vec{r}_a)\psi_k(\vec{r}_a)$ and $q_{jl}(\vec{r}_b) = \psi_i^*(\vec{r}_b)\psi_k(\vec{r}_b)$, respectively are the equivalent point charges at $\vec{r}_a$ and $\vec{r}_b$ and N is the number of atoms in the simulation domain. So, the kernel $|\vec{r}_a - \vec{r}_b|^{-1}$ represents the repulsion between the charges q_{ik} and q_{jl}. The integral J, therefore, can be interpreted as the electrostatic "Coulomb"

interaction between all possible *point* charges (located at atomic positions of the crystal). Or in other words, it is the energy required to place N point charges q_{jl} in a field due to N point charges q_{ik} located at $\vec{r} = \{1, 2, ..., N\}$, or the r^{-1} interaction.

The "Coulomb" or r^{-1} interaction is a far-field potential and is long range since the decay of potential is slower than r^d, where d is the dimensionality of the system. The decay of the potential is sufficiently slow that all possible interactions between *point* charges must be accounted for and hence, the computational complexity of such a computation is $O(N^2)$. This is called an N-body problem and appears commonly in many fields like molecular dynamics, celestial mechanics, plasma physics and fluid dynamics, where the particle-particle interactions have a similar form as equations 2.6 and 2.7.

Several algorithms have been proposed to reduce the computational complexity of an N-body problem to $O(NlnN)$ or $O(N)$. These are based on Ewald summation methods; Fourier Transforms of Ewald methods like Particle-Particle Particle-Mesh P3M, Particle Mesh Ewald PME, Smooth Particle Mesh Ewald SPME, Fast Fourier Poisson FFP; quad-trees and oct-trees like Barnes-Hut, Fast Multipole Method FMM. This work proposes using the act-tree based Fast Multipole Method, FMM to evaluate the integrals J and K in 2.6 and 2.7 necessary in evaluating ACI Hamiltonian elements.

Fast Multipole Method, FMM was introduced by Greengard and Rokhlin and has been acclaimed as one of the top 10 algorithms of the 20th century. Unlike some of the other common methods, the method can be applied to both periodic and non-periodic systems and can be applied to a non-uniform distribution of particles with a fairly high accuracy. It reduces the computational complexity to $O(NlnN)$ and further to $O(N)$ for a uniform distribution of particles, which is typically the case for integrals J and K in equations 2.6 and 2.7 since the *point* charges q_{ik} and q_{jl} are defined at the atomic positions of the host crystal material.

Fast Multipole Method (FMM) is an oct-tree based method to solve the n-body problem [46]. The algorithm reduces the complexity of the problem from $\mathcal{O}(N^2)$ to

$\mathcal{O}(NlogN)$ or $\mathcal{O}(N)$ and can be applied to both periodic and non-periodic systems even with a non-uniform distribution of particles with relatively high accuracy. The method is based on arithmetic simplification of a function F that includes interactions between every two points in a system of N particles. Considering, for the sake of simplicity, a the function F evaluated at point x_i including its interactions with all other points in the system as

$$F(x_i) = \sum_{j=1}^{N} a_j (y_i - x_j)^2 \tag{2.9}$$

For an N-particle system, the evaluation of function F at all points $x_i = 1toN$ has a complexity of $\mathcal{O}(N^2)$. However, the mathematical structure of the equation can be taken advantage of to split the equation as

$$F(x_i) = \left(\sum_{j=1}^{N} a_j \right) x_i^2 + \left(\sum_{j=1}^{N} a_j x_j^2 \right) - 2x_i \left(\sum_{j=1}^{N} a_j x_j \right) \tag{2.10}$$

where each of the three terms in the brackets can be computed as $\mathcal{O}(N)$ for summation over i and the function F is evaluated at each of the j points as $\mathcal{O}(N)$. So the total complexity of the computation is reduced from $\mathcal{O}(N^2)$ to $\mathcal{O}(N)$+$\mathcal{O}(N)$ or simply $\mathcal{O}(N)$. FMM employs this idea of analytically manipulating a series to accelerate its summation [47].

Extending the idea to a Coulomb kernel for the n-body problems, the potential at any point $\vec{r}_i$ due to all other point charges in the system is given as

$$\phi(\vec{r}_i) = \sum_{j=1}^{N} q(\vec{r}_j) \frac{1}{|\vec{r}|} \tag{2.11}$$

where $\vec{r} = \vec{r}_i - \vec{r}_j$ is the distance between source particle j and target particle i. If a set of n particles around $\vec{r}_j$ are grouped into a cluster such that their centre is at $\vec{r}_c$, then the distance of this cluster from the target particle i is $\vec{r}_i - \vec{r}_c = \vec{R}$ and from the source particle j is $\vec{r}_c - \vec{r}_j = \vec{r} - \vec{R}$. It is important to note that the distance $\vec{R}$ is independent of j and the distance $\vec{r} - \vec{R}$ is independent if i. This separation of source and target variables allows to write the above expression for a Coulomb kernel as

$$\frac{1}{\vec{r}} = \sum_{n=0}^{p} \frac{1}{n!} \left(\vec{r} - \vec{R} \right)^n \frac{\partial^{(n)}}{\partial \vec{R}} \frac{1}{R} \tag{2.12}$$

where p is the order of Taylor expansion for r^{-1} about $\vec{R}$. Using the above expansion, the potential at point i due to the cluster of particles centered at $\vec{r}_c$ is given as

$$\begin{aligned}\phi(\vec{r}_i) &= \sum_{j=0}^{N} \frac{(\vec{r}_j)}{\vec{r}} \\ &= \sum_{j=0}^{N} (\vec{r}_j) \sum_{n=0}^{p} \frac{1}{n!} \left(\vec{r} - \vec{R}\right)^n \frac{\partial^{(n)}}{\partial \vec{R}} \frac{1}{R} \\ &= \sum_{n=0}^{p} \frac{\partial^{(n)}}{\partial \vec{R}} \frac{1}{R} \sum_{j=0}^{N} \frac{1}{n!} q(\vec{r}_j) \left(\vec{r} - \vec{R}\right)^n\end{aligned} \tag{2.13}$$

where the terms with $\vec{R}$ are independent of j as explained and have been pulled out of summation over j. The terms remaining within the summation over j are the multipole expansion terms, monopole for n=0, dipole for n=1, quadrupole for n=2 and so on.

As explained in [48], a system of N particles can be grouped into clusters of different hierarchy. The maximum number of particles in the cluster of lowest hierarchy can set to a fixed number n depending on the desired accuracy of the result. The net effect of all the n particles in a cluster, at a point located far away from the cluster, can be approximated by an effective potential and is mathematically represented by a local expansion. This potential depends only on particles inside the cluster and the above summation converges for points inside the cluster. For a particle located in one cluster, its interactions with the other particles in the same cluster and the particles in the nearest-neighbor clusters are treated as near-field particle-particle interactions. But the particles in the far away clusters are sufficiently far enough such that their effect can be approximated by a far-field particle-cell interaction using a multipole expansion. A detailed explanation of the algorithm has been well described in [46] for reference.

FMM is implemented in ACI to evaluate the integrals J and K in equations 2.6 and 2.7. As seen from Fig. 2.4, for a relative error of 0.02, FMM is faster than direct evaluation of integrals using the brute-force method for different number of atoms N in the domain. Tunable parameters to achieve a balance of simulation time and accuracy

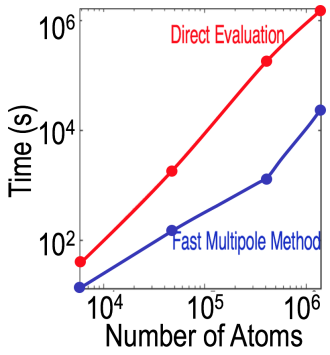

Fig. 2.4. Performance of ACI, using direct evaluation of integrals with brute-force method and fast multipole method FMM for a relative error of 0.02, shows about 100x speed-up achieved with FMM.

include (1) number of particles in a cell, the higher the number, greater the accuracy; (2) order of expansion, of the spherical harmonics that are used as a basis in Taylor expansion of r^{-1}; (3) multipole criterion, indicates the critical distance beyond which the particle-cell interactions can approximate the net potential due to all particles in the cell. It must be noted that, while FMM improves the performance of ACI for a reasonable accuracy, certain quantum computing devices demand a resolution of few-electron eigenenergies of the order of neV and for this high accuracy, there is no specific advantage in using FMM against the brute-force method. Rather, the brute-force method can be parallelized much more efficiently and is preferred when a high accuracy in the solution is desired.

2.4 Summary

Atomistic Configuration Interaction, ACI is a many-body approach based on atomistic tight-binding (TB) and full configuration interaction (FCI). Atomistic TB is successfully demonstrated to model multi-million atom systems with complex geometries, incorporating the band structure effects and atomsitic effects of defects and interfaces, but for a single-electron system. FCI is an exact method that captures all

electron-electron interactions; Coulomb repulsion between electrons, exchange interactions and correlations. Therefore, for a realistic few-electron system, using atomistic TB with FCI, in ACI can give a fairly accurate estimate of the few-electron energy spectrum and configurations of the few-electron states. ACI, however, is computationally demanding due to the several 6-dimensional integrals required to be evaluated over the entire simulation domain. The ACI code is implemented in NEMO to be massively parallelized over thousands of cores, using shared memory models and multi-threading; and adapting clever algorithms like FMM that reduce the complexity of the intensive computations. In the following chapters, ACI is first benchmarked against experimental data and later employed in gaining deep physical insights of different quantum computing systems. ACI has further been used in exploring novel donor based architectures [49], in studying two-electron spin relaxation times T_1 [50] and in modeling two- and three-electron double quantum dot hybrid qubits in silicon.

3. EXPERIMENTAL VALIDATION OF ACI

The contents of this chapter are going to be submitted to a peer-reviewed journal. On acceptance into a peer-reviewed journal, copyright will belong to the journal publisher. Part of the content is available on arXiv at arXiv:1703.04175 (2017) and arXiv:1706.09261 (2017).

Single electron spin qubits in semiconductors have been successfully demonstrated experimentally [11, 12] and atomistic tight-binding simulations are shown to explain and predict several of these high profile experiments like the single atom transistor and world's thinnest nanowire [27, 28]. Towards scalable quantum computers, the next big challenge is a coherent control of two qubits. The two qubit operations, for single-electron spin qubits, rely on the exchange of information between two electron spins.

Two qubit SWAP gate, for example, in Kane qubit architecture [51] Fig. 3.1(a) is a bias on the J-gate (middle-gate or exchange-gate) that couples the two electron spin qubits bound to two phosphorous donors. As seen from the potential profile in Fig. 3.1(b), when the J-Gate is OFF, the two electron spins are isolated, confined strongly to the two phosphorous donors. Applying a J-Gate bias lowers the potential barrier between the donors allowing the electron wavefunctions to interact strongly, Fig. 3.1(c). Due to the exchange coupling, the electron spins rotate with respect to each other. If the bias is applied precisely for a π rotation of the electron spins, SWAP operation is achieved. The electron spins rotate in response to each other's magnetic field thus achieving a SWAP of the electron spins. Turning the J-Gate OFF returns the electron spins to the donors and isolates them from each other as shown in Fig. 3.1(d).

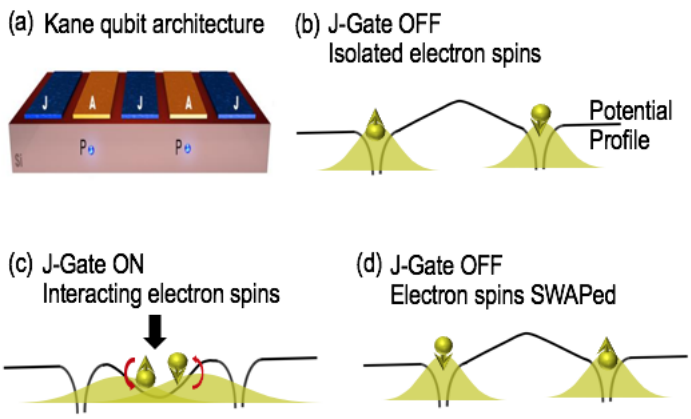

Fig. 3.1. Simple illustration of the two qubit SWAP gate. (a) Kane qubit architecture [51] (This figure has been taken from Ref. [49]). (b) Isolated electrons bound to phosphorous donors for single qubit operations. (c) J-Gate bias lowers the potential barrier between electrons and allows electrons to freely evolve in the presence of each other's magnetic field. (d) Turning OFF J-Gate precisely after π rotation (SWAP) of the spins to create the barrier and isolate the electrons.

For a precise SWAP operation, it is critical to pulse the J-Gate to achieve exactly a π rotation of the electron spins. The speed of rotation of these spins depends on how strongly the electrons interact with each other, or in other words, the electron exchange energy. It is, therefore, important to understand the two-electron exchange interactions towards two qubit gate operations in electron spin qubits.

Several experiments are being actively pursued to understand and measure the electron-electron interactions. Prof. Sven Rogge's group at the Center for Quantum Computation and Communication Technology (CQCCT), UNSW has been studying electrons bound to dopant atoms in an STM set-up; energy spectra, images of these electron wavefunctions and interactions between two electrons. In this work, few-electron spectra from ACI are benchmarked against the experiments for (1) a single phosphorous donor in bulk silicon binding two electrons, i.e. a doubly charged donor, (2) a single doubly charged arsenic donor located close to the silicon interface, probed by an STM, (3) a phosphorous donor pair binding one electron each, i.e. a neutral

donor pair, located close to the silicon interface probed by an STM, and (4) small GaAs quantum dots.

The important metrics in studying the few-electron spectrum that will be referred to in this work are two-electron charging energy, two-electron binding energy, exchange energy and addition energy. When the single-electron states of the system are spin degenerate, a second electron can be added to the same ground state as the first, but with an anti-parallel spin. However, the total energy of this two-electron state is not just twice the single-electron ground state energy E^{1e}. Coulomb repulsion between the two electrons increases the energy of this two-electron state. Therefore, the two-electron energies of relevance are defined taking these electron interactions into consideration. Addition energy E_A is defined as the energy it takes to add one more electron to an n-electron system, $E^{(n+1)e} - E^{ne}$. Two electron charging energy E_{CE} is the "extra" energy that is needed to add a second electron to a single-electron system $E^{2e} - 2E^{1e}$. Two-electron binding energy E^{2e}_{BE} is the energy with respect to the conduction band minimum of the host material $2E_{CB_{min}} - E^{2e}$. It is, therefore, the energy that is required to ionize the quantum dot or donor. And lastly, exchange energy J is the energy splitting between the two-electron spin antisymmetric singlet and spin symmetric triplet states, respectively. It must be noted that this exchange energy J is different from the exchange interactions and Coulomb integrals J discussed in the previous chapters. Since it is conventional to call this singlet-triplet splitting as exchange J, the same notation will be continued to be used for exchange energy, unless mentioned otherwise.

3.1 Phosphorous donor in bulk silicon

A single donor binding two electrons, D^- center, is particularly important in dopant based quantum computing devices in silicon. Transport experiments in single atom transistors indicate the presence of a bound singlet D^- ground state [27] that

is strongly affected by the gates due to a low binding energy, 1.7 meV for negative phosphorous and 2.05 meV for negative arsenic [52].

The spherically symmetric Coulomb potential of the donor when disrupted by the tetrahedral crystal potential leads to valley-orbit coupling. This valley-orbit coupling lifts the valley degeneracies of the donor states and thus modifies the electronic spectrum of the single donor. The six-fold valley degeneracy of the ground state of donor Coulomb confinement Fig. 3.2(a), the 1s manifold, is broken by the local crystal field into a singlet with A1 symmetry, a triplet with T2 symmetry and a doublet with E symmetry.

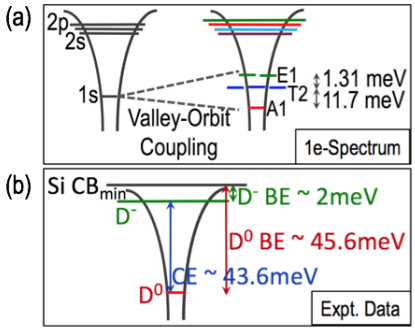

Fig. 3.2. Energy spectrum of single phosphorous donor in bulk silicon. (a) Single-electron spectrum. Degeneracy of hydrogenic 1s-like states of a donor Coulomb confinement potential, broken into valley-orbit singlet, triplets and doublets (A_1, T_2 and E respectively) by the tetrahedral crystal symmetry of the host material. (b) Binding and charging energies of donor bound electrons from experimentally observed D^0 and D^- states.

The theoretical treatment of donors in silicon presents several challenges. The singularity of donor potential is complicated by the multi-valley states in silicon host. Approximations based on effective mass theory have been used before to study neutral and negative donor centres [53,54] but they fail to capture valley splitting exactly and the effects of interfaces and defects in the system. Theoretical models used to study D centers so far have been greatly simplified. An accurate determination of the donor energy spectrum in silicon is challenging due to (1) electron mass anisotropy

in the material, (2) strong intervalley coupling in the multivalley host, (3) an incomplete knowledge of impurity potential at the donor core, and (4) the electron-electron interactions considering the correction in dielectric screening at small separations. Binding energies and degeneracies of these 1s states of a neutral phosphorous donor in silicon, D^0 center, determined using semi-empirical tight-binding model have been successfully validated against experimental values [55]. In this work, ACI is used to determine the two-electron states of a single phosphorous donor in bulk silicon.

Optical experiments on a bulk phosphorous donor in silicon indicate the presence of a bound singlet D^- state with a binding energy approximately 2.0meV below the conduction band minimum, corresponding to a charging energy of 43.6meV [56], as shown in Fig. 3.2(b). ACI calculation of a bulk phosphorous donor D^- in silicon is presented in Fig. 3.3. It must be noted that although we treat phosphorous donor specifically here, the same method can be used on other shallow group V donors in silicon and the results will qualitatively be the same. Fig. 3.3(a) shows the charging energy of the two-electron state as a function of the number of spin-resolved D^0 atomic states in the basis. Including only $1s$-like D^0 states in the ACI method gives a significantly overestimated charging energy of 71.8meV as shown in Fig. 3.3, indicating an incomplete basis. With the inclusion of $2s$, $3s$ and $4s$-like D^0 states in the basis, the charging energy converges to 46.0meV. It must be noted that the binding energies are evaluated with reference to the conduction band minima of bulk silicon at 1.131355eV obtained from a bulk bandstructure calculation [57]. A finite box size of the simulation domain, in this case 35nm x 35nm x 35nm causes interface confinement effects on the excited donor states. Therefore, the system is not really bulk, only bulk-like, which leads to higher orbital energies due to increased confinement. This is one of the reasons for slightly higher charging energy of 46.0meV relative to the 43.6meV measured in the optical experiments. From the wavefunction, the D^- state with 46.0meV charging energy is observed to be localized to the donor. Within the approximations of tight-binding basis orbitals, discretized tight-binding wavefunctions, central-cell corrected donor potential and truncated single-electron

basis set, ACI still gives a fairly close charging energy of the negative phosphorous donor in bulk. Hence, the excited donor states in the manifold of $2p$, $2s$, $3s$ and so on, which are typically ignored in most calculations, are crucial for the solution of the two-electron donor state.

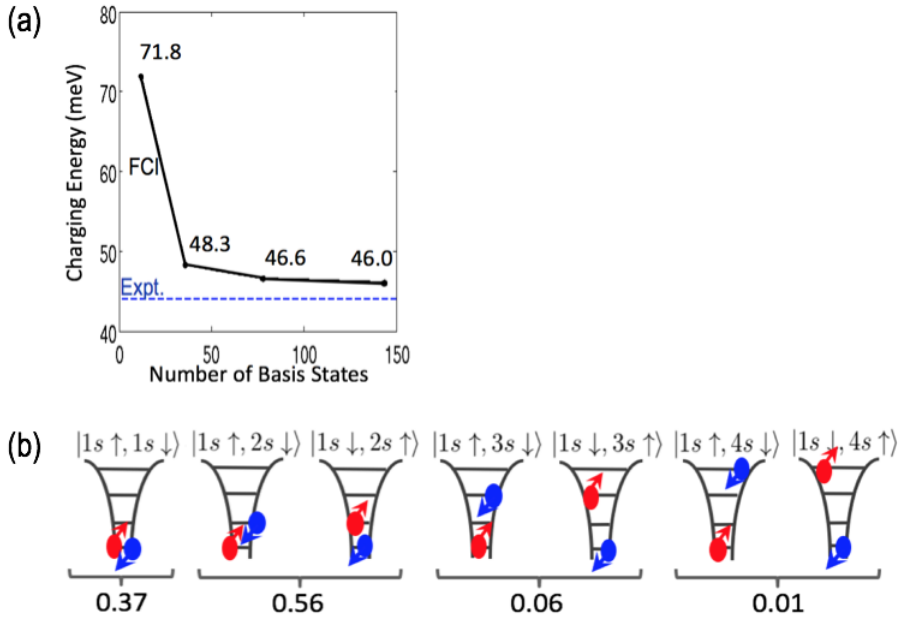

Fig. 3.3. Negative phosphorous donor D^- states in bulk silicon from ACI. (a) D^- charging energy of phosphorous donor in silicon converges towards the experimentally observed value of 43.6meV [56] with increasing number of single electron states in the FCI basis. The data points correspond to the inclusion of $1s$, $2s$, $3s$ and $4s$-like states in the basis. (b) Two-electron D^- ground state. Numbers indicate the probability that the system is in each of the configurations. One of the electrons is always in the D^0 ground state, $1s$-like state with A_1 symmetry. The second electron occupies $2s$, $3s$ or $4s$-like excited states also of A_1 symmetry. The excited state splittings corresponding to 2s, 3s, 4s are magnified in the schematic relative to Fig. 3.2(a) to portray the electronic configurations clearly. Also, the T_2 and E_1 states are omitted for simplicity.

Fig. 3.3(b) shows the two-electron configurations that compose the spin anti-symmetric singlet D^- ground state of a phosphorous donor in silicon as obtained from ACI. The spin symmetric triplet states in the excited two-electron donor spec-

trum are not bound for a single donor in bulk silicon. From the two-electron ACI wavefunction in Fig. 3.3(b), it is seen that the probability of the D^- state existing in $|1s\uparrow, 1s\downarrow\rangle$ configuration is only 37%. $1s$-like states are therefore not sufficient to describe the D^- ground state. There is a significant contribution of 56% from $|1s\uparrow, 2s\downarrow\rangle$ and $|1s\downarrow, 2s\uparrow\rangle$ states and including the $2s$-like states in the FCI basis corrects the charging energy. Contributions from $2s$, $3s$ and $4s$-like D^0 states to the D^- ground state suggests that the negative donor has strong Coulomb correlations. A complete basis for such a system is huge and requires at least 150 single-electron spin states. For the employed basis and simulation domain, the calculated ACI charging energy of 46.0 meV approaches the value of 43.6 meV in bulk. The remaining discrepancy is small and might be reduced by increasing basis size or simulation domain size. However, increasing either is beyond the scope of the present work.

As can be seen from Fig. 3.3(b), all the contributing electronic configurations have anti-parallel spins, consistent with the net spin of a singlet state. Moreover, we find that one of the electrons of D^- always occupies the $1s$-like state with A_1 symmetry, the D^0 ground state. It is favorable for the other electron to have the same valley symmetry which increases the electron correlations, thus lowering the energy of the two-electron singlet state. From the ACI solution of the ground state, we find that $2s$, $3s$ and $4s$-like D^0 states that contribute to the D^- singlet have all A_1 symmetry. Therefore, for the bulk donor, T_2 and E states with different valley symmetries are not found to contribute to the D^- ground state. It must be noted that the D^- state from ACI is somewhat like the Chandrasekhar-like wavefunction with appropriate valley symmetries, if the second orbital of the Chandrasekhar wavefunction can be thought of as a hybrid of the $1s$, $2s$, $3s$ and $4s$ orbitals.

The significant contributions of the excited Slater determinants to the D^- state show strong electronic correlations based on orbital and valley symmetries. Such correlations cannot be captured with a mean-field treatment of the problem. ACI, therefore, provides a comprehensive description and valuable insights into the two-electron

states of donors in silicon taking into account the electron-electron interactions arising from excited configurations that cannot be ignored for a correlated system.

3.2 Arsenic donor in silicon probed by STM

A single donor coupled to a single-electron quantum dot is one of the key building blocks of quantum computing architectures. There are proposals to use a quantum dot to mediate interactions between donor bound electron spins [58] via the tunnel coupling between each donor and the quantum dot. In Kane architecture, electron spins bound to two donors are coupled by exchange interactions tuned with the application of J-Gate bias, as described in the introduction of this chapter. However, these exchange interactions are highly sensitive to the donor locations [59,60]. J. Salfi et al. from Prof. Rogge's group at CQCCT were able to experimentally demonstrate the possibility of reducing this sensitivity of exchange interactions to the precise donor separation by using a coupled single-electron quantum dot and donor system.

Resonant tunneling experiments [61], in imaging the wavefunctions of electrons bound to dopant atoms in a lightly doped silicon region, have a heavily doped silicon as an electron reservoir. Arsenic donors are placed precisely in a silicon lattice using STM lithography. To allow an STM probing of these donors, they are only few nm deep from the silicon interface.

For the tip-induced quantum dot used in the above experiment, the single-electron binding energy E_{BE}^{1e} is measured to be 50meV at V=-0.3V tip bias and the two-electron charging energy E_{CE}^{2e} to be 50meV at V=-0.4V bias, far away from the donor. These experimentally measured values are used to calibrate the environmental parameters i.e. tip radius r, tip height h, tip opening angle θ and the depth of reservoir d, as shown in Fig. 3.4. The geometry and electrostatics of the tip-vacuum-silicon-reservoir system is set up in COMSOL. The potential profile extracted from COMSOL is input to the single-electron atomistic simulation tool NEMO3D to obtain the eigenstates of the tip-induced quantum dot.

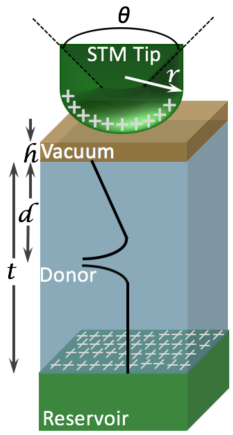

Fig. 3.4. Schematic of a donor probed by an STM tip. Metallic reservoir and metallic tip significantly alter the electrostatics at donor location. Tunable parameters in ACI simulation: tip radius r, tip height h, tip opening angle θ and the depth of reservoir d.

Table 3.1 shows that the E^{1e}_{BE} of the tip-induced quantum dot is less sensitive to h and θ, changing only by 0.3meV for 10° change in θ and by 4meV for 0.05nm change in h but is effected more by r and t.

Two-electron charging energy E^{2e}_{CE} of the tip-induced quantum dot is calculated for the selected values of r and t, parametrized to match the experimentally observed value of E^{1e}_{BE}=50meV. Atomistic configuration interaction, ACI is used to evaluate the two-electron states of the tip-induced quantum dot. Table 3.2 shows that two particular cases, (r=5nm and t=16nm) and (r=9nm and t=10nm) give a E^{2e}_{CE} that agrees well with the experimentally measured value of 50meV at V=-0.4V.

Based on the E^{1e}_{BE} and E^{2e}_{CE} calculated for the tip-induced dot, the following are the parameters estimated: θ=45, h=0.15nm, r=5nm and t=16nm. An STM set-up with these parameters is used to study the two-electron arsenic donor spectrum and its wavefunctions. Using metrology [62], the depth of the donor under study is estimated to be 5.75a0 or 6.75a0, from its single-electron image in real space and Fourier space. Following the same procedure as above, except including the arsenic donor in the tight-binding simulations now, the binding energies for single and two electrons, E^{1e}_{BE}

Table 3.1.
Single-electron binding energies E_{BE}^{1e} for different environmental parameters of the tip-induced quantum dot.

r=5nm h=0.15nm t=10nm V=-0.3V	θ=45°	θ=55°
E_{BE}^{1e}	31.0meV	31.3meV

r=5nm θ=45° t=10nm V=-0.3V	h=0.1nm	h=0.15nm	h=0.2nm	h=0.25nm
E_{BE}^{1e}	34.0meV	32.6meV	28.6meV	26.7meV

θ=45° h=0.15 t=10nm V=-0.3V	r=5nm	r=7nm	r=9nm
E_{BE}^{1e}	31.0meV	41.3meV	50.3meV

r=5nm θ=45° h=0.15nm V=-0.3V	t=10nm	t=16nm	t=20nm
E_{BE}^{1e}	31.0meV	46.5meV	50.5meV

Table 3.2.
Two-electron charging energies E^{2e}_{CE} for different environmental parameters of the tip-induced quantum dot.

θ=45° h=0.15nm	r=5nm t=16nm	r=9nm t=10nm
E^{1e}_{BE} at V=-0.3V	46.5meV	50.3meV
E^{2e}_{CE} at V=-0.4V	52.2meV	55.8meV

and E^{2e}_{BE}, are calculated to be 120.68meV and 63.97meV, respectively for a 5.75a0 deep arsenic donor and 115.94meV and 62.63meV for 6.75a0 deep donor. The ionization energy is estimated to be 56.7meV and 53.31meV for the dot+donor system, with the donor 5.75a0 and 6.75a0 deep respectively, and 46.5meV for the dot alone. The difference between the ionization energies of the donor+dot and the dot-only system, which is the energy saved when the tip is over the donor, is 10.2meV (5.75a0) and 6.81meV (6.75a0). These numbers agrees well with the experimental value of 5.5meV (when the tip is approximately 10nm from the donor and not at infinity, for the measurement of ionization energy of tip-induced quantum dot), especially for the 6.75a0 deep donor.

One of the key considerations in this analysis was the inclusion the effect of silicon-vacuum-tip interfaces and dielectric mismatches, using the method of images charges on the screening of electron-electron interactions, as described in the previous chapter on methodology. The two-electron charging energy is significantly reduced due to this additional screening effect. This was critical in obtaining a close quantitative match with the experimental data. For electrons bound to an arsenic donor located close to the interface, the effect of the electrostatics of the interface cannot be ignored.

3.3 Phosphorous donor pair in silicon probed by STM

Donor pairs are the building blocks of the one of the first propoals on donor based quantum computing architectures in silicon, the Kane qubit [51]. As discussed in previous sections, the two-qubit gate operations rely on exchange interactions between electrons. These interactions are associated with the energy splitting between the two-electron spin antisymmetric singlet and spin symmetric triplet states, the exchange energy J. For a precise qubit gate operation, it is therefore critical to have a comprehensive understanding of how the exchange energy J is effected by the donor separations and their crystallographic orientations. J. Bocquel et al. from Prof. Rogge's group at CQCCT have employed STM spectroscopy to investigate several phosphorous donor pairs with different separations and separation directions, to understand the correlation between the exchange energy J and the valley oscillations [63].

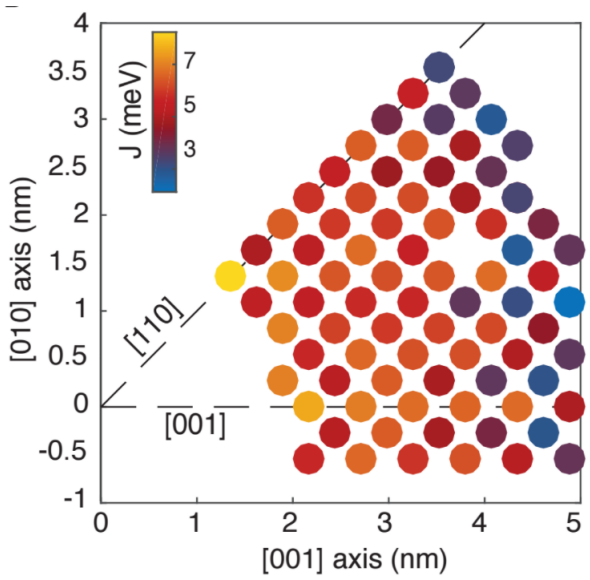

Fig. 3.5. Exchange energies of neutral donor pairs as a function of donor separation and relative position between the [001] and [110] crystallographic axes for donors $4.5a_0$ deep from ACI.

Singlet-triplet splitting that can be resolved experimentally from the spectroscopy, or the spatially resolved differential conductance dI/dU spectrum of the donor pair, is limited by the operating temperature. At 5K, the energy resolution cannot be less than 0.5meV and this sets an upper limit on donor separations to 5nm for donors located 4.5a0 from the silicon surface. This limit is obtained from theoretical simulations of a donor pair with two electrons using atomistic configuration interaction, ACI. Fig. 3.5 shows the exchange energy J, on a color scale, for a 4.5a0 deep phosphorous donor pair, assuming one of the donors fixed at (0,0) and the other donor at the lattice sites indicated by the circles. J falls below 1meV for separations larger than 5nm, hence, only lattice sites where the donor separation is less than 5nm along any direction have been shown in the figure. It must be noted that the exchange energy J decreases overall with increasing separation (albeit rather slowly) and oscillates with a change in direction of separation from [100] to [110].

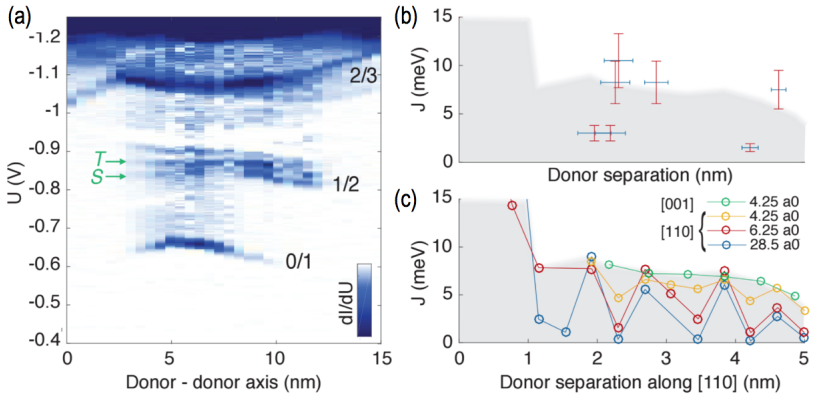

Fig. 3.6. Exchange in phosphorous donor pairs in silicon. (a) Spatially resolved differential conductance dI/dU spectrum of two exchange coupled P donors. Single-, two- and three-electron states in the spectrum can be identified from the curvatures of dI/dU vs. x. Exchange energy is defined as the energy difference between the singlet ground state S and first excited triplet T state. (b) Energy splitting between ground state and first measured excited state extracted from several two-donor dI/dU spectra plotted as a function of donor separation. (c) Exchange energies as a function of donor separation along the [110] axis and for different donor depths, obtained from ACI.

To study the two-electron neutral donor pairs, J. Bocquel et al. from Prof. Rogge's group have fabricated a large variety of sub-surface phosphorous donor pairs, targetted to be 4.5a0 deep, at different separations and orientations, using STM lithography techniques. J is extracted from the spatially resolved differential conductance dI/dU spectrum of the donor pair as shown in Fig. 3.6(a), where S and T are the two-electron singlet and triplet states. The two-electron states do not have a curvature on the U vs. x plot as they are charge neutral. The single- and three-electron states, however, are seen to have a curvature due to a net positive and negative charge, respectively. Fig. 3.6(b) shows the extracted J for several of these pairs as a function of donor separation r, with error bars. The uncertainity arises from the difficulty in precisely determining the donor locations for closely-spaced donors. Fig. 3.6(c) is the same result of J vs. r from ACI for donors at different depths and along the direction of maximum J oscillation, [110]. The results from experiments and theory are in fairly good agreement with each other, with respect to the oscillations in J and the order of magnitude of J.

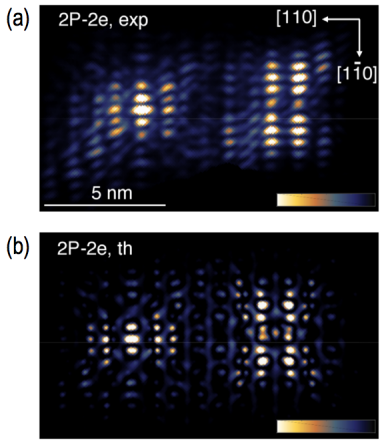

Fig. 3.7. Quasi-particle wavefunction image of neutral donor pair corresponding to 2e→1e transition. (a) Experimental image from STM current map. (b) Theoretical images using two-electron wavefunctions from ACI and STM image calculation [62] for the same donor locations as in (a).

Furthermore, Prof. Rogge's group images the quasi-particle wavefunction of the neutral donor pair, corresponding to the 2e→1e transition. Fig. 3.7(a) shows the STM image of one such pair. The donor coordinates are extracted from this image using the spatial metrology technique [62] by M. Usman et al. from Prof. Hollenberg's group at CQCCT. Two-electron ground-state singlet wavefunction is obtained from ACI for the corresponding donor locations, in the Slater determinant basis, and is used to determine the quasi-particle image of the two-electron state using the method described in reference []. Fig. 3.7(b) shows the quasi-particle wavefunction image from atomistic simulations that agrees closely, in real space, with the experimental image in Fig. 3.7(a).

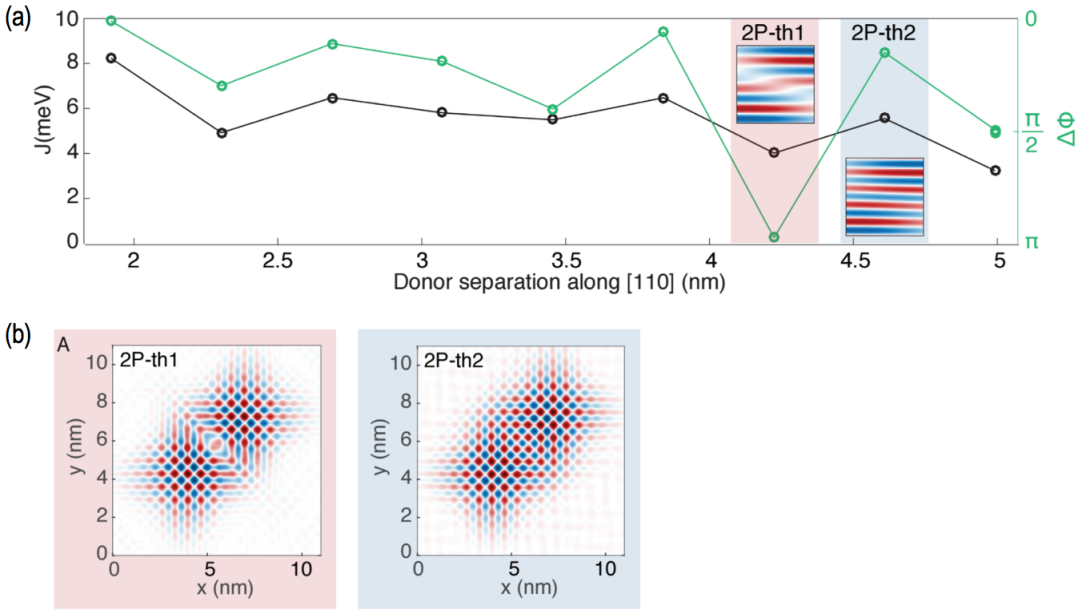

Fig. 3.8. Correlation bewteen exchange and valley interferences. (a) Destructive and constructive valley interferences for two different donor pairs separated by 4.2nm and 4.6nm along [110], respectively. (b) Exchange J (black) and phase difference between the valley interferences (in green) with donor separation. Destructive interferences lead to smaller overlap of electron wavefunctions and thus, lower exchange.

ACI simulations are also used to understand the correlation between exchange J and valley interference by J. Bocquel et al [63]. Black curve in Fig. 3.8(a) represents the exchange J with donor separation r along [110] for donors 4.5a0 deep. To understand the oscillations in exchange, for the two points corresponding to the local minima and maxima of J vs. r (highlighted in red and blue, respectively), the real space valley oscillations are extracted from the ACI two-electron quasi-particle wavefunction in Fig. 3.8(b). 2P-th1 shows destructive valley interferences causing lower exchange and 2P-th2 shows constructive valley interferences leading to a higher exchange in Fig. 3.8(a). The phase difference between the two valley oscillations in Fig. 3.8(b) is plotted on the J vs. r figure, and the correlations between J and valley interferences is thus demonstrated from atomistic ACI simulations.

3.4 GaAs quantum dots

The electronic spectrum of electrostatic quantum dots in GaAs is remarkably different from silicon. In silicon, the confined quantum dot orbital states are coupled to the X-point valley states of the multi-valley silicon host, which introduces additional features in its electronic properties. GaAs, however, is a single-valley host at the Γ-point and there is no valley degree of freedom, unlike silicon. Therefore, filling electrons in a GaAs single-valley artificial atom is only orbital and spin dependent. Shell filling observed in these artifical atoms is similar to the atomic shell filling [64].

GaAs quantum dot is defined in a heterostructure, where GaAs is sandwiched between two large bandgap materials, like AlGaAs or InGaAs. The band profile is such that a 2D electron gas (2DEG) is formed at the GaAs interface as shown in Fig. 1.2(a). Lateral confinement of electrons is achieved with top gates, as discussed in previous chapters. Tarucha et al. obtained the shell structure of a GaAs quantum dot, in a double-barrier heterostructure, tunnel coupled to the doped GaAs leads to add electrons to the dot. At zero magnetic field, the addition energy is estimated

with varying number of electrons in the dot. Similar to atomic shell structure, the addition energy is unusually large when each of the shells are completely full.

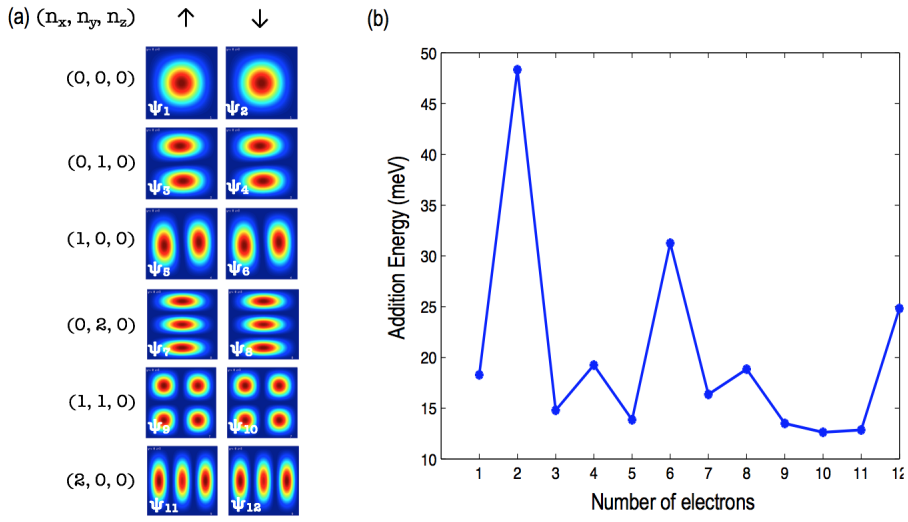

Fig. 3.9. Shell filling in a GaAs quantum dot. (a) Single-electron wavefunctions of an elliptic GaAs quantum dot with an electric field of 5 MV/m along Z and dot curvatures of 10^{-3} and 0.75x10^{-3} along X and Y directions. The lowest 12 wavefunctions shown here correspond to 0^{th} n_z mode. (b) Addition energy with increasing number of electrons in the dot from ACI, using Slater determinants from the basis shown in (a).

Atomistic configuration interaction, ACI is used in a qualitative theoretical study of the shell filling in a GaAs quantum dot. The simulation domain is much smaller 30nm x 30nm x 15nm compared to the experimental set up due to the computational burden in simulating many-electron system for a realistic GaAs quantum dot. The confining potential is assumed to be linear, due to a constant electric field of 5 MV/m along Z, perpendicular to the 2DEG and parabolic/harmonic in the lateral directions X and Y. Since GaAs is a small effective mass material, in order to ensure the electron wavefunctions are not affected by the artificial domain boundries, a very large lateral confinement potential, with curvatures of 10^{-3} and 0.75x10^{-3} along X and Y directions are used. Using different curvatures generates an elliptical dot, instead of circular dot. This is because, for a circular dot, n_z=0 mode has the following (n_x, n_y)

spin-degenerate modes: {(0, 0)}, {(0, 1), (1, 0)}, {(0, 2), (1, 1), (2, 0)}, {(0, 3), (1, 2), (2, 1), (3, 0)}, ...and so on, where the states in { } are the (n_x, n_y) configurations that are degenerate in energy. It is difficult to resolve such large number of degeneracies using Block Lanczos eigensolver since it needs a larger block size and takes longer to converge. Elliptical dots are therefore used to break these degeneracies in orbital states of the quantum dot, for example, (0,1) and (1,0) have different energies now since the X confinement is stronger than the Y confinement. Single electron states are obtained from NEMO3D in a 20-band $sp^3d^5s^*$ basis, the lowest 12 as shown in Fig. 3.9(a) and are used to construct n-electron Slater determinants for n=2 to n=12. ACI Hamiltonian is diagonalized in the Slater determinant basis to obtain n-electron eigenenergies and eigenstates.

$$
\begin{aligned}
\left|\Psi^{2e}\right\rangle &= 0.992\,|\psi_1,\psi_2\rangle \\
\left|\Psi^{3e}\right\rangle &= 0.980\,|\psi_1,\psi_2,\psi_3\rangle \\
&= 0.980\,|\psi_1,\psi_2,\psi_4\rangle \\
\left|\Psi^{4e}\right\rangle &= 0.953\,|\psi_1,\psi_2,\psi_3,\psi_4\rangle \\
\left|\Psi^{5e}\right\rangle &= 0.959\,|\psi_1,\psi_2,\psi_3,\psi_4,\psi_5\rangle + 0.010\,|\psi_1,\psi_3,\psi_4,\psi_5,\psi_{10}\rangle \\
&= 0.959\,|\psi_1,\psi_2,\psi_3,\psi_4,\psi_6\rangle + 0.010\,|\psi_2,\psi_3,\psi_4,\psi_6,\psi_9\rangle \\
\left|\Psi^{6e}\right\rangle &= 0.940\,|\psi_1,\psi_2,\psi_3,\psi_4,\psi_5,\psi_6\rangle + 0.012\,|\psi_1,\psi_3,\psi_4,\psi_5,\psi_6,\psi_{10}\rangle \\
&\quad + 0.012\,|\psi_2,\psi_3,\psi_4,\psi_5,\psi_6,\psi_9\rangle \\
\left|\Psi^{7e}\right\rangle &= 0.922\,|\psi_1,\psi_2,\psi_3,\psi_4,\psi_5,\psi_6,\psi_8\rangle + 0.017\,|\psi_1,\psi_3,\psi_4,\psi_5,\psi_6,\psi_8,\psi_{10}\rangle \\
&\quad + 0.012\,|\psi_2,\psi_3,\psi_4,\psi_5,\psi_6,\psi_8,\psi_9\rangle \\
&= 0.922\,|\psi_1,\psi_2,\psi_3,\psi_4,\psi_5,\psi_6,\psi_7\rangle + 0.017\,|\psi_1,\psi_3,\psi_4,\psi_5,\psi_6,\psi_7,\psi_{10}\rangle \\
&\quad + 0.012\,|\psi_2,\psi_3,\psi_4,\psi_5,\psi_6,\psi_7,\psi_9\rangle \\
\left|\Psi^{8e}\right\rangle &= 0.893\,|\psi_1,\psi_2,\psi_3,\psi_4,\psi_5,\psi_6,\psi_7,\psi_8\rangle + 0.026\,|\psi_1,\psi_3,\psi_4,\psi_5,\psi_6,\psi_7,\psi_8,\psi_{10}\rangle \\
&\quad + 0.026\,|\psi_2,\psi_3,\psi_4,\psi_5,\psi_6,\psi_7,\psi_8,\psi_9\rangle \\
\left|\Psi^{9e}\right\rangle &= 0.831\,|\psi_1,\psi_2,\psi_3,\psi_4,\psi_5,\psi_6,\psi_7,\psi_8,\psi_9\rangle + 0.069\,|\psi_1,\psi_2,\psi_3,\psi_4,\psi_5,\psi_6,\psi_7,\psi_8,\psi_{13}\rangle \\
&\quad + 0.026\,|\psi_1,\psi_3,\psi_4,\psi_5,\psi_6,\psi_7,\psi_8,\psi_9,\psi_{10}\rangle + 0.031\,|\psi_2,\psi_3,\psi_4,\psi_5,\psi_6,\psi_7,\psi_8,\psi_9,\psi_{13}\rangle \\
&= 0.831\,|\psi_1,\psi_2,\psi_3,\psi_4,\psi_5,\psi_6,\psi_7,\psi_8,\psi_{10}\rangle + 0.069\,|\psi_1,\psi_2,\psi_3,\psi_4,\psi_5,\psi_6,\psi_7,\psi_8,\psi_{14}\rangle \\
&\quad + 0.031\,|\psi_1,\psi_3,\psi_4,\psi_5,\psi_6,\psi_7,\psi_8,\psi_{10},\psi_{14}\rangle + 0.026\,|\psi_2,\psi_3,\psi_4,\psi_5,\psi_6,\psi_7,\psi_8,\psi_9,\psi_{10}\rangle
\end{aligned}
\tag{3.1}
$$

For the GaAs quantum dot described above, Fig. 3.9(b) shows the addition energy E_A with increasing number of electrons n in the dot. E_A is lower when the first shell is filled at n=2, when the second shell is filled at n=6 and when the third shell is filled at n=12. With increasing number of electrons, the ACI Hamiltonian size increases exponentially. The Hamiltonian is a 18564 x 18564 dense matrix for a 6-

electron system using a basis of 18 single-electron states. Diagonalization of these dense matrices limits the number of electrons and the basis size that can be used to solve the multi-electron states of the system accurately. However, for the GaAs quantum dot, the ACI results agree qualitatively with Tarucha et al. Moreover, the configurations of the ground state, for different number of electrons, are obtained from ACI in equation 3.1, where the ψ_i are the single electron states shown in Fig. 3.9(a).

It must be noted that in the absence of magnetic field, with even number of electrons in the system, the lowest two states are singlet-triplet-like while with odd number of electrons, the lowest two states have different spin configurations but are degenerate in energy. ACI, thus, not only gives the n-electron energy spectrum but also their configurations as shown in equation 3.1 to understand the shell filling in artificial atoms. Single-valley GaAs quantum dot is a simple system used to qualitatively benchmark the results from ACI against experimental data.

3.5 Summary

Two-qubit gate operations in single-electron spin qubits rely on electron exchange interactions. It is, therefore, critical to gain deeper insights into the physics of these interactions. Atomistic configuration interaction, ACI is employed to evaluate these interactions in electrons bound to phosphorous and arsenic donors in silicon and to electrostatic gate-defined quantum dots in GaAs. The two-electron metrics, i.e binding energies E_{BE}, charging energies E_{CE}, addition energies E_A or the exchange energies J, obtained from ACI simulation results are benchmarked against available experimental data for the above mentioned systems. A close agreement with experiments, especially for dopant based qubits, not only provides sufficient validation of the ACI method in estimating the electron interactions but also endorses its applications in evaluating the performance of novel qubit architectures or in gaining deeper insights into the physics of the qubit devices.

4. PHYSICAL INSIGHTS FROM ACI

The contents of this chapter are going to be submitted to a peer-reviewed journal. On acceptance into a peer-reviewed journal, copyright will belong to the journal publisher. Part of the content is available on arXiv at arXiv:1703.04175 (2017).

Single negative donors and neutral donor pairs, located close to the silicon surface, are extremely important towards a comprehensive understanding the dopant based quantum computing architectures [11,51,65–67]. Their vicinity to the surface enables an STM probing of these devices, as discussed in the previous chapter, to study the electron wavefunctions and the energy spectra. For negative phosphorous, the effect of electric fields, depth of the donor and the electrostatics of the interfaces on the two-electron states of the donor is determined using ACI. For neutral donor pairs, approximate methods like Heitler-London and Hartree-Fock are used to evaluate the exchange. In this work, ACI simulations show that these approximate models are invalid for a large range of donor separations. Moreover, for closely spaced donors, these methods are even inaccurate. ACI is used to investigate donor pairs at varying separations along different crystal directions.

4.1 Sub-surface negative phosphorous donor in silicon

Donors close to the oxide-silicon interface are important for silicon quantum computing for a number of reasons. The first signature of single donor orbital states and their Stark shift were detected in single donors located less than 10nm from an oxide-silicon interface in FinFETs [65]. In this regime, the donor is strongly tunnel coupled to states confined at the interface, and a gate voltage can ionize the electron adiabatically through intermediate donor-interface/donor-dot hybrid states [68, 69].

There have been proposals to use this system to form hybrid donor dot qubits where electrons are pulsed to the interface states for two-qubit operations with enhanced exchange couplings and pulsed back to the donors to take advantage of the long quantum memory in donor bound states [70, 71]. Recent experiments have also manipulated multiple electrons between donors and interface states [72] in a hybrid donor-dot setting.

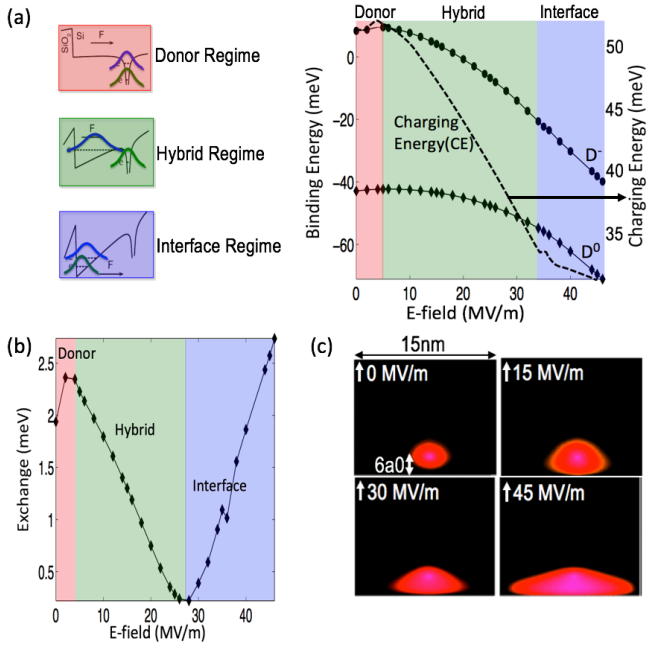

Fig. 4.1. Effect of electric field on the charging and exchange energies of a P donor in silicon, 6a0 deep from oxide-semiconductor interface; (a) Schematic of possible regimes with increasing E-fields when both electrons are localized at donor, one electron at donor and other hybridized with interface, both electrons at the interface. D^0 and D^- binding energies and derived D^- charging energy (dashed line) with increasing electric fields. (b) Exchange or singlet-triplet splitting of the D^- state. (c) Two-electron densities of D^- singlet ground state from full configuration interaction for different confinement regimes (on a *log* scale). Delocalization of two-electron states is observed at large fields.

Two-electron charging energies of sub-surface dopants have also been observed to be around 30meV [65] in stark contrast to bulk charging energies close to 44meV. This

also enables the possibility of bound triplet states, which to our knowledge have not been observed in bulk donors, and a measurable singlet-triplet (exchange) splitting. Here, we show ACI can explain these experimental observations. We will also show the change in exchange coupling in a two-electron donor state as a function of an applied bias for donors close to interfaces, which is of relevance in hybrid donor-dot qubits.

The binding energies of both D^0 and D^- states have been plotted in Fig. 4.1(a). The difference between the two is the charging energy of D^-, shown by a dashed line on the right axis. Singlet-triplet splitting or the exchange energy, with varying electric field is shown in Fig. 4.1(b). Exchange depends on the overlap of the single electron wavefunctions. Charge densities of the D^- ground state are shown in Fig. 4.1(c) revealing the spatial spread of two-electron states under different confinement regimes.

Increasing the electric field causes the excited donor states to hybridize with the interface well states. One of the electrons is pushed towards the interface leading to delocalization of the electron, as shown in the schematic for hybrid regime in Fig. 4.1(a). With increasing field in this regime (at moderate electric fields) the delocalization increases which lowers the charging energy. This delocalization also lowers the overlap of the electron wavefunctions, thus decreasing the exchange with increasing fields.

At large fields, both electrons dominantly occupy the ground state of the interface well, strongly confined along the vertical field direction and weakly confined by the donor potential laterally. The decrease in orbital energies of single-electron states with increasing field leads to the decrease in the charging energy of D^- in the interfacial regime. However, the increase in wavefunction overlap of the two electrons localized at the interface causes an increase in exchange with increasing electric field. The donor regime, at low electric fields, is similar to the interface regime, where both electrons are localized at the donor instead of the interface.

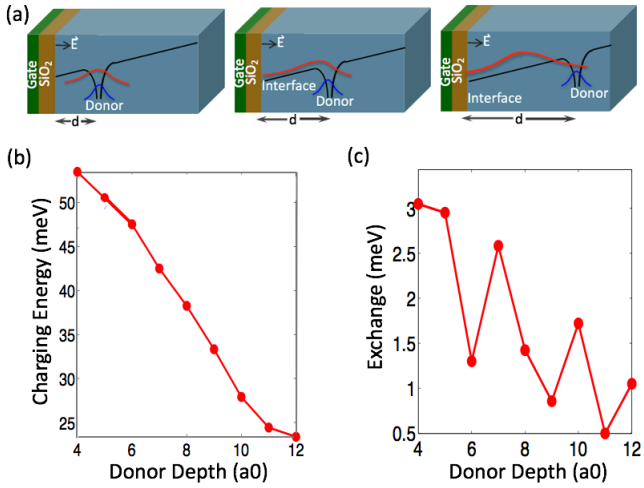

Fig. 4.2. Effect of the donor depth on the charging and exchange energies; (a) Schematic of increasing electron delocalization with increasing donor depth at a moderate electric field of 15MV/m, in the hybrid regime. (b) D^- charging energies. (c) Singlet-triplet splitting of D^-. (a0=0.543nm for silicon).

D^- charging and exchange energies varying with depth of the P donor are shown in Fig. 4.2 corresponding to the hybrid regime. At 15MV/m field, as can be understood from the schematic in Fig. 4.2(a), increasing the depth of the donor increases the delocalization of one of the electrons, thus lowering the charging energies as seen in Fig. 4.2(b). This also leads to a smaller overlap of electron wavefunctions and therefore, exchange also decreases with increasing donor depth as shown in Fig. 4.2(c). The oscillations in exchange are due to the difference in phase of the Bloch wavefunctions of the two electrons.

Donors close to the interface have dielectric mismatches arising from Si-SiO_2 and SiO_2-metallic gate interfaces. A reservoir of heavily doped silicon substrate also creates a dielectric mismatch as shown in Fig. 4.3(a). The reservoir is particularly important in scanning tunneling experiments when the highly doped silicon layer is located 10-20nm away from the donor [61, 73]. For MOS-like devices, the device contacts are in proximity to the donor too and ideally the image charges in contacts

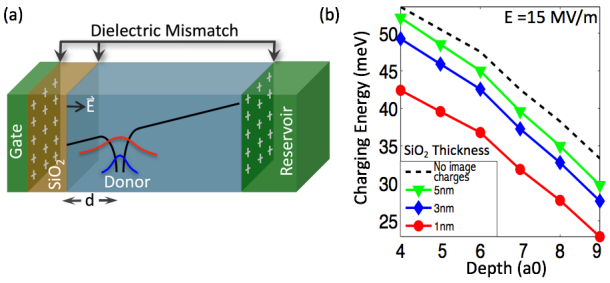

Fig. 4.3. Hetero-interface effects on a donor charging energy; (a) P donor in silicon, located close to Si-SiO_2-metal interface and to a heavily doped reservoir, important in resonant tunneling experiments. (b) Charging energy of D^- at 15MV/m E-field for different oxide thicknesses. A thinner dielectric increases the screening of electronic repulsions by the metallic gate, leading to lower charging energies.

must be accounted for as well, which have been ignored in this work [74]. Metallic and oxide interfaces close to an electron affect the electrostatics of the system and screen the electron-electron repulsions, thus lowering the two electron energies of the system. Fig. 4.3(b) shows the effect of the electrostatics of interfaces on the charging energy of D^- state. As the thickness of the SiO_2 oxide layer decreases, the Si-SiO_2-metal interface becomes more metallic in nature and screens the electron interactions resulting in decreasing the two electron charging energy. The effect of the image charges is seen mainly as an offset in the charging energy.

For sub-surface donors, the charging and exchange energies are shown to be sensitive to the depth of the donors from the Si-SiO_2 interface, applied electric fields and the electrostatics of the interfaces, from the ACI simulations. The charging and exchange energies of D^- are lower for deeper donors under moderate electric fields, typically the regime of interest for hybrid donor-dot architectures, but the exchange energies show small oscillations, less than an order of magnitude, with increasing depth. Moreover, in spite of the increased computational complexity in including the effect of electrostatics of interfaces on electron interactions, they are significant in evaluating the charging energies of shallow donors in the vicinity of oxide and metallic

interfaces. The understanding of two-electron states from this work may be useful in the realization of hybrid donor-dot qubit architectures.

4.2 Phosphorous donor pair in silicon

Donor pairs are the building blocks of the first donor-based quantum computing architecture proposed by Bruce Kane [51]. Two qubit operations in these architectures, like SWAP gate discussed in the previous chapter, require two electron spins to exchange information. The exchange interaction between electron spins can be tuned electrically with a J gate bias, as shown in Fig. 3.1. A precise control of this exchange interaction between electron spins bound to two dopant atoms in silicon is critical in a two-qubit operation.

4.2.1 Approximate methods for electron exchange interactions

Electron interactions are typically evaluated using approximate methods like Heitler-London method or Hartree-Fock method. Heitler-London approximation assumes the electrons are strongly correlated and uses a two-electron wavefunction described as

$$\psi(r_1, r_2) = [\phi_L(r_1)\phi_R(r_2) + \phi_R(r_1)\phi_L(r_2)]\,(\uparrow_1\downarrow_2 - \downarrow_1\uparrow_2) \tag{4.1}$$

where ϕ_L and ϕ_R are orbitals localized to the left and right donors, respectively. The electrons are assumed to be localized to these orbital states which is valid when the donor separation is large. For closer donor separations, Hartree-Fock approximation is typically used which includes the configurations where both electrons are localized on the same donor, i.e. the ionic terms. The two-electron Hartree-Fock wavefunction is represented as

$$\begin{aligned}\psi(r_1, r_2) = {} & [\phi_L(r_1)\phi_L(r_2) + \phi_L(r_1)\phi_R(r_2) + \phi_R(r_1)\phi_L(r_2) \\ & + \phi_R(r_1)\phi_R(r_2)]\,(\uparrow_1\downarrow_2 - \downarrow_1\uparrow_2)\end{aligned} \tag{4.2}$$

Together, these two approximations have been used to evaluate exchange interactions in donor molecules at different donor separations.

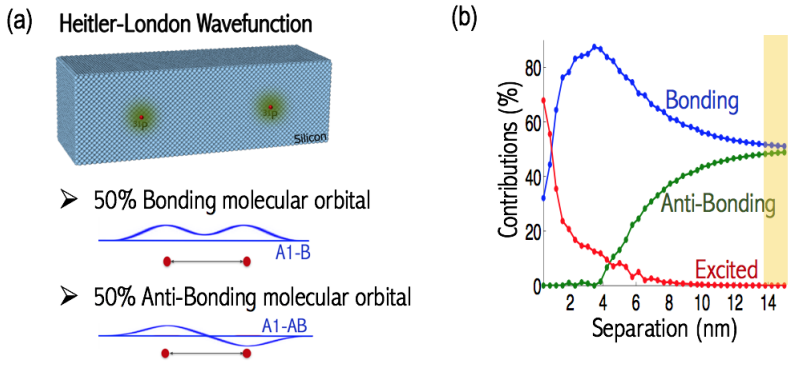

Fig. 4.4. Heitler-London Wavefunction. (a) Well separated phosphorous donors (red atoms) in silicon (blue atoms) close to the surface and localized electron orbital states (green) on each donor. Heitler-London wavefunction constitutes 50% contribution from the bonding state, $\phi_B = \phi_L(r) + \phi_R(r)$ and 50% from the anti-bonding state, $\phi_{AB} = \phi_L(r) - \phi_R(r)$, where ϕ_L and ϕ_R are orbitals localized to the left and right donors, respectively. (b) ACI simulations of the two-electron neutral donor pair, located $4.5a_0$ below the silicon surface, separated along [110]. Contributions from bonding states, anti-bonding states and all remaining (excited) states obtained from the ACI wavefunction. Highlighted region, for donor separation larger than 13nm, is the Heitler-London regime where the bonding and anti-bonding contributions are equal and there are no contributions from any other (excited) states of the donors.

Atomistic configuration interaction, ACI accurately determines electron interactions and is used to study the exchange in donor pairs at varying donor separations from 0.5nm to 15nm. For a donor pair located close to the silicon surface and separated along [110], the contributions of the molecular bonding states and anti-bonding states are extracted from the ACI wavefunction in Fig. 4.4(b). The two-electron Heitler-London wavefunction when represented in the basis of molecular orbitals, instead of orbitals localized to the donor atoms, has equal contributions from bonding and anti-bonding states, as shown in Fig. 4.4(a). As seen from Fig. 4.4(b), the

Heitler-London approximation is valid only at large donor separations, more than 13nm.

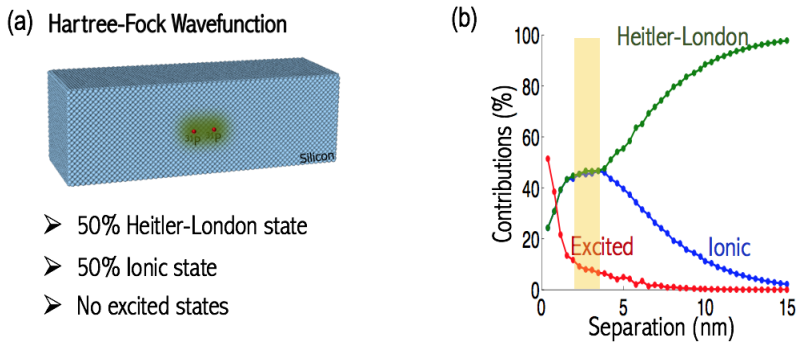

Fig. 4.5. Hartree-Fock Wavefunction. (a) Closely spaced phosphorous donors (red atoms) in silicon (blue atoms) close to the surface and localized electron orbital states (green) on each donor. Hartree-Fock wavefunction constitutes 50% contribution from the Heitler-London state, $\phi_L(r_1)\phi_R(r_2)+\phi_R(r_1)\phi_L(r_2)$ and 50% from the ionic state, $\phi_L(r_1)\phi_L(r_2)+\phi_R(r_1)\phi_R(r_2)$, where ϕ_L and ϕ_R are orbitals localized to the left and right donors, respectively. (b) ACI simulations of the two-electron neutral donor pair, located $4.5a_0$ below the silicon surface, separated along [110]. Contributions from Heitler-London states, ionic states and all remaining (excited) states obtained from the ACI wavefunction. Highlighted region, for donor separation between 3nm to 4nm, is the Hartree-Fock regime where the Heitler-London and ionic contributions are equal. However, there is a significant contribution from the excited states of the donor that is not captured in the Hartree-Fock approximation.

For the same ACI wavefunction, the contributions from Heitler-London like terms and ionic terms are extracted instead of the bonding-antibonding terms and plotted in Fig. 4.5(b). The large donor separations are Heitler-London dominant terms where the ionic configurations almost do not exist. The Hartree-Fock approximation is assumed to be valid at small donor separations where the weights of the Heitler-London terms and ionic terms are equal, as shown in Fig. 4.5(a). However, as shown in Fig. 4.5(b), this is true only for donor separations between 3-4nm and still is only an approximation since at these separations, there is a significant contribution from

the excited states that are not included in the Hartree-Fock wavefunction. From ACI, the validity regimes for the Heitler-London and Hartree-Fock approximate methods, typically used in evaluating exchange in donor pairs in silicon for two-qubit operations, have been determined. These approximations are not valid over a large range of donor separations and more accurate methods like ACI must be used to evaluate electron interactions for the two-qubit gate operations.

4.2.2 Suppressed exchange oscillations for sub-surface donors

Heitler-London approximation has typically been used to evaluate exchange interactions for donor pairs in bulk silicon separated along different directions. It is well known from effective mass and atomistic Heitler-London methods [59, 75, 76] that exchange decays exponentially with increasing donor separation along [100]. But the donors separated along [110] show violent oscillations in exchange, that inhibits a precise gate control of a two-qubit operation based on exchange interaction between electrons.

The exchange oscillations for donors separated along [110] are significantly suppressed for sub-surface donors. ACI results in Fig. 4.6 show the variation in exchange with donor separation from 4nm to 15nm along [110] for donors at three different depths, $3.5a_0$, $6.5a_0$ and $28.5a_0$(or bulk). For donors separated in the X-Y plane, the exchange oscillations arise from valley interferences of the X and Y valleys. At $28.5a_0$, the X, Y and Z valleys of the donors are equally populated and therefore, a small change in X-Y separation of the donor affects the X-Y valley interferences and thus, exchange. However, for $3.5a_0$ deep donors, no oscillations in exchange are observed on a log scale. This is because, the silicon interface increases the confinement along the direction perpendicular to the interface, Z in this case. The confinement increases the energies of the X and Y valleys more than the Z valleys since the X and Y valleys have lower effective mass along Z direction. Therefore, the lower energy states of the sub-surface donors are Z-valley dominant. The X and Y valley populations are

small and therefore, the X-Y valley interferences have a much smaller effect on the exchange. Suppressed exchange oscillations provide a better gate control for the two qubit operation that is robust against the donor separation in the X-Y plane.

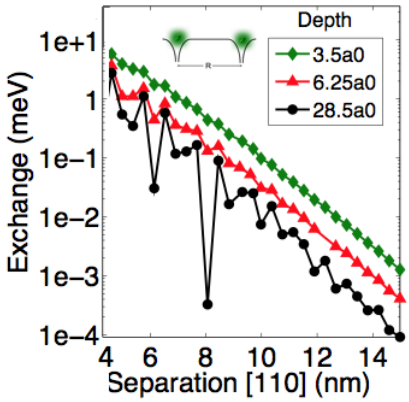

Fig. 4.6. Suppressed exchange oscillations. Exchange for donor pairs separated by R from 4nm to 15nm along [110] at different depths from the silicon surface from ACI. Oscillations in exchange are suppressed for donors close to the surface due to valley repopulation.

4.2.3 Exchange saturation at small donor separations

The exchange evaluated for large donor separations using Heitler-London method is known to increase exponentially with decreasing donor separations, albeit oscillations in certain directions. For closer donors, it is reasonable to expect the exponential trend to continue since the electrons feel each other more strongly with decreasing donor separation. ACI allows to explore these very close donor separation regimes for a quantitative estimation of the electron exchange interactions, unlike the approximate methods discussed in the previous sections that are either invalid or inaccurate at these separations. Fig. 4.7(a) shows exchange with donor separation from 0.5nm to 15nm along [110] for donors at three different depths, $3.5a_0$, $6.5a_0$ and $28.5a_0$(or bulk). Contrary to the expected exponential increase in exchange with decreasing

donor separation, exchange saturates for donors closer than a critical separation distance. At these small separations, the A1 anti-bonding state of donor pair anti-crosses with the T2 bonding state, as shown in Fig. 4.7(b). This changes the symmetry of the donor molecule since the two electrons now occupy the A1 and T2 bonding states instead of A1 bonding and A1 anti-bonding states. Changing the donor separation does not effect the splitting between A1 and T2 bonding states as much as between A1 bonding and A1 anti-bonding states. Thus, when the two-electron states mainly consist of the bonding states, exchange saturates with donor separation.

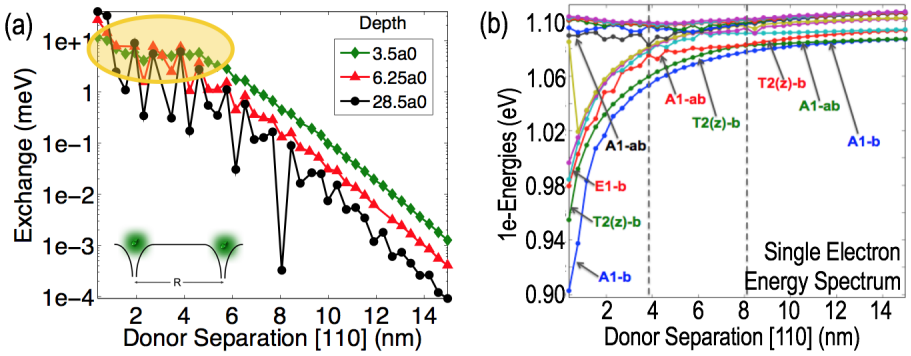

Fig. 4.7. Exchange saturation for closely spaced donors. (a) Exchange for donor pairs separated by R, ranging from 0.5nm to 15nm along [110] at different depths from the silicon surface obtained from ACI. For closely spaced donors, i.e. separation less than 4nm, exchange saturates due to a change in symmetry of the two-electron state of the donor pair. (b) Single-electron spectra for the donor pairs in (a). A1 anti-bonding and T2 bonding states anti-cross at roughly 4nm, which changes the symmetry of the two-electron state, leading to exchange saturation as seen in (a).

4.2.4 Variation in exchange with donor depths

The suppression of exchange oscillations for shallow donor pairs is shown in Fig. 4.7 for larger donor separations from 4nm to 15nm along [110]. The close donor separation regime, where exchange saturates, the exchange still oscillates due to the a finite population of the X and Y valleys of the donors. As discussed in the ear-

lier sections, the X and Y valley populations increases with increasing depth of the two donors and therefore, a small displacement in one of the donor positions can significantly change the X and Y valley interferences and thus, the exchange.

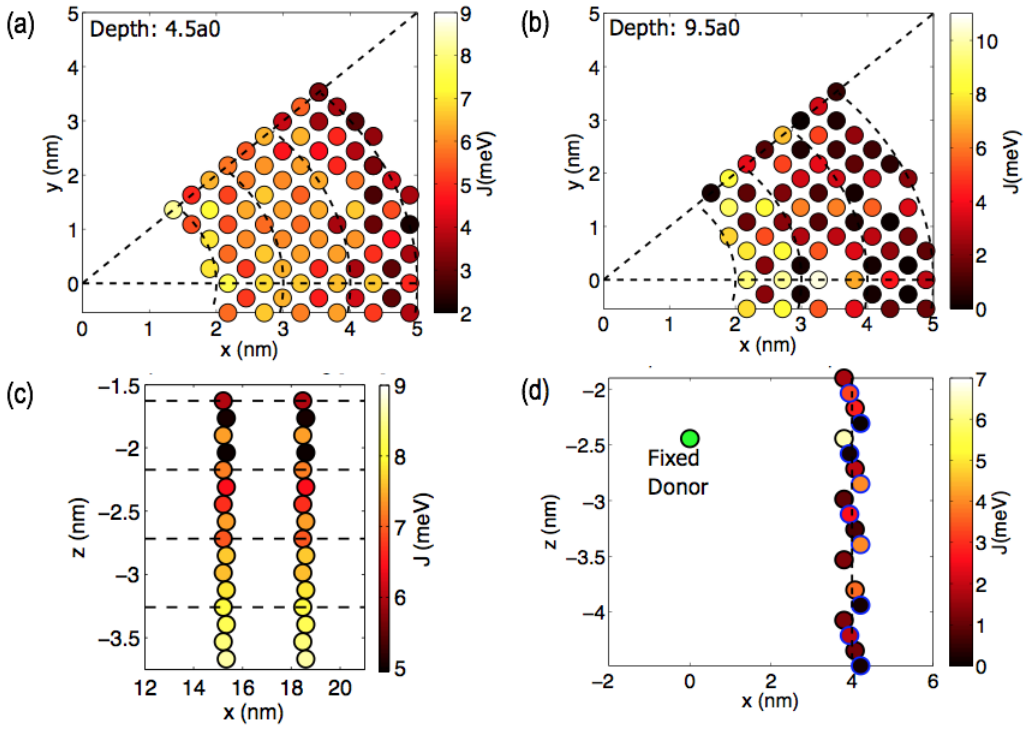

Fig. 4.8. Exchange with donor depths. Circles indicate lattice positions for donors and color bar shows the value of exchange for a specific donor configuration. (a) $4.5a_0$ deep coplanar donors with one of the donors at (0,0) and the second donor is at lattice sites marked in circles. Exchange oscillates around the same order of magnitude with donor separation distance and direction. (b) $9.5a_0$ deep coplanar donors. Oscillations in exchange are higher, over 1-2 orders of magnitude, due to an increased population of X and Y valleys for donors farther from the interface. (c) Donors at 3nm separation along [100]. Shallow donors have smaller exchange due to reduced overlap of the wavefunctions of the two electrons in the X, Y directions resulting from increased hybridization of donor states and the interface well states. Oscillations in exchange are higher for shallow donors because of increased Z-valley population. (d) One donor fixed at z=-$4.5a_0$ and second donor varied in depth. Large exchange oscillations from Z-valley interferences.

ACI simulations on a large number of coplanar donor pairs (i.e. both donors at the same depth from the surface) including all possible donor configurations for separations ranging from 2nm to 5nm are done for two different donor depths $4.5a_0$ and $9.5a_0$, as shown in Fig. 4.8(a) and Fig. 4.8(b), respectively. The exchange oscillations, with both the donor separation distance and direction, are small - about the same order of magnitude, for the shallow pair at $4.5a_0$ in Fig. 4.8(a). However, at $9.5a_0$ depth, the oscillations are over 1-2 orders of magnitude, both with the separation distance and direction. Fig. 4.8(c) shows the exchange variation with the depth of coplanar donors, for a fixed separation of 3nm along [100]. Whether exchange increases or decreases with depth of the pair depends on the X and Y valley interferences for a fixed donor separation. As seen from the figure, the oscillations in exchange are highest when the donors are shallow. As the depth increases, the Z-valley population of the donor states decreases and thus, for a fixed separation, the oscillations in exchange are smaller. But the magnitude of exchange increases with the depth of the donors. This is because for shallow donors, the donors states are hybridized with the interface well states, which increases the real space wavefunction spread in the Z direction and decreases the spread along the X, Y directions. Since the donors are separated in the X-Y plane and the overlap of electron wavefunctions is smaller due to smaller wavefunction spread, exchange is smaller for shallower donors.

For a more comprehensive understanding of the effect of the depths of the donors on the electron exchange interaction in a donor pair, the relative depths of the donors must be considered as well. When there is a difference in the relative depths of the two donors, the Z-valley interferences are effected by this difference. Due to high Z-valley population in sub-surface donors, a small change in relative donor depths can lead to a significant change in exchange. Fig. 4.8(d) shows exchange with increasing depth of one donor relative to the other donor fixed at 4.5a0 from the silicon surface, is sensitive to these Z-valley interferences.

4.2.5 Monotonic charging energies

The two-electron charging energy does not oscillate like exchange but changes rather monotonically with the donor separations and remains nearly constant with the donor separation direction, as seen from Fig. 4.9(a). This can potentially be used to get a closer estimate of the donor positions in an STM experiment, over the spatial metrology, for donors estimated to be located at the same depth. Moreover, as seen from Fig. 4.9(b), the two-electron charging energy increases with the depth of the donor pair. At shallower depths, the donor states hybridize with the well states, thus lowering the energies of the bonding-like states. The charging energy saturates to the bulk values as the depth of the donor pair increases.

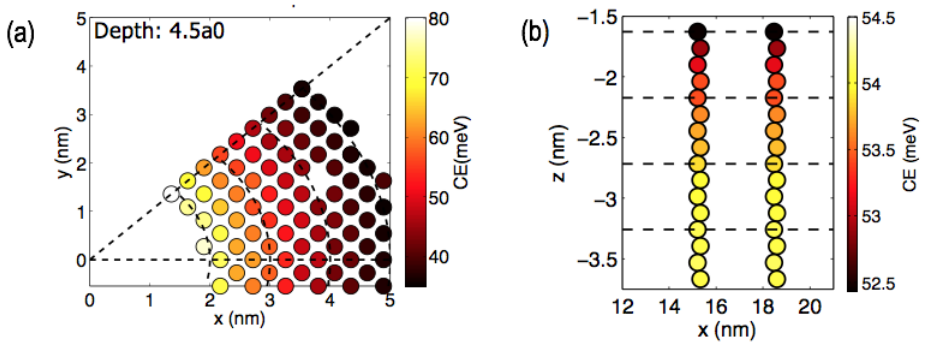

Fig. 4.9. Monotonically varying two-electron charging energies of donor pairs, with separation and depth. Circles indicate lattice positions for donors and color bar shows the value of exchange for a specific donor configuration. (a) $4.5a_0$ deep coplanar donors with one of the donors at (0,0) and the second donor is at lattice sites marked in circles. Charging energy changes monotonically as compared against exchange in Fig. 4.8(a). (b) Donors separated by 3nm along [100]. Charging energy increases with depth due to decreasing hybridization with interface states.

A fairly thorough study of exchange and two-electron charging energy in neutral donor pairs is presented in this work, especially for closely spaced donors (2nm-5nm separation), that can be probed with an STM set-up, to gain a deeper insights into the effect of valley physics on two-electron states.

4.3 Summary

Two-electron states of single donors and donor pairs are important in read-out of single electron spin qubit and in two-qubit manipulation. ACI modeling of sub-surface negative phosphorous donors in silicon shows that with increasing electric fields and decreasing depths of the donor from the silicon surface, the hybridization of the donor states with the interface well states increases. This has different effect on the two-electron charging energies and exchange. Moreover, since the donor is close to the interface, the dielectric mismatches also screen the electron interactions and alter the two-electron spectrum.

Exchange in neutral donor pairs evaluated using approximate methods is shown to be invalid for a large range of donor separations. For closely space donors, typically in STM experiments, these methods are not accurate and hence ACI is used to study the close separation regimes. While exchange increases exponentially with decreasing donor separation, below a certain separation, exchange is shown to saturate from ACI simulations, due to a change in the symmetry of the two-electron states. The oscillations in exchange with donor separation along [110] are also shown to be suppressed for shallow donors located close to the interface. This is due to increase in Z-valley population that makes exchange less immune to donor separation along X-Y directions. Exchange oscillations are also studied with varying donor depths. Finally, the two-electron charging energies are shown to be more monotonic, as compared to the exchange, with donor separations.

5. EXCHANGE BASED DONOR BOUND ELECTRON SPIN QUBITS

Electron spins bound to phosphorous donors in silicon are promising spin qubits for quantum information processing. Donor bound electron spins have been shown to have exceptionally long coherence times, often exceeding seconds at cryogenic temperatures [21], making the spins of these electrons attractive for quantum information processing. Coherent manipulation of a single electron spin on a phosphorus donor in silicon has been demonstrated via microwave pulses that drive transitions between the $|\uparrow\rangle$ and $|\downarrow\rangle$ spin states [11]. AC magnetic fields, however, can limit the gate operation frequencies for single spin qubits and introduce noise sources from the microwave transmission lines [14]. Alternately, oscillating electrical pulses operate at gigahertz frequencies and yield high frequency qubit manipulations but in the absence of spin-orbit coupling, cannot induce transitions between single spin qubit states $|\uparrow\rangle$ and $|\downarrow\rangle$. However, electrical pulses can couple two spins via an exchange interaction between the two electrons.

Electrical tuning of exchange interaction is exploited in a qubit architecture defined by two electron spins, a singlet-triplet qubit. Exchange drives high-frequency qubit rotations by coupling the pair of electron spins localized on two tunnel-coupled quantum dots. For a full two-axis qubit control, rotation about a second axis is typically achieved with a nuclear Overhauser field [15] or an integrated micromagnet [77]. A resulting gradient magnetic field creates a different local environment for the two electrons and determines the relative phase evolution of the decoupled spins. These

transverse fields can cause inhomogeneous dephasing of the electron spins and ideally must be turned *off* when the electron spins are coupled by an exchange pulse.

Instead of relying on a gradient magnetic field for qubit rotation about a second axis, an exchange-only qubit architecture employs electrically controlled exchange interactions for rotations about *both* axes [29–31]. This requires coupling two different pairs of electrons via exchange interactions and therefore at least three electrons confined to three quantum dots. For a linear left-middle-right quantum dot geometry, exchange interactions between electron spins in the left-middle dots and middle-right dots drive rotations about two different axes. Fast gate rotations at gigahertz frequencies can be achieved by tuning exchange via exchange-only EO [29], resonant-exchange RX [32,33] or always-on exchange-only AEON [78]. Complexity of controlling multiple electron spins for a single qubit manipulation is compromised for the high qubit operation speed.

While coherent control of the singlet-triplet [15,77,79–87] and exchange qubits [29, 32, 33, 88, 89] has already been demonstrated successfully in electrostatically-defined dots, realization of multiple electron spin qubits, confined to dopant atoms in silicon, is constrained mainly by (a) loosely confined singlet state and non-availability of bound triplet states, which is critical as explained later and; (b) oscillations in exchange with donor separation [59,75,76,90,91]. In both two-spin and three-spin architectures, the qubit initialization and read-out regimes require loading two electron spins on the same donor. But the two-electron ground state of a phosphorous donor in bulk silicon is only 1.7meV [56] from the conduction band minimum and bound triplet states have not been reported. Oscillations in exchange with donor separation, both distance and direction, also put stringent requirements on precise placement of donors in silicon and a precise gate control for a qubit operation.

To address these challenges, singlet-triplet and exchange-only qubit architectures based on *sub-surface* donors, in the proximity of a gate-oxide-semiconductor interface, in silicon are proposed in this work. An electron bound to a sub-surface donor is confined by a triangular well perpendicular to the interface due to gate bias and by

the donor potential laterally at moderate electric fields. The size of the dot depends on the depth of the donor, the confinement decays as Coulombic r^{-1}, causing a weakening confinement with increasing donor depth. Strongly confined electron wavefunctions in donor-dots, as against electrostatically-defined dots, are expected to be less sensitive to the effects of interface roughness or charge noise and have improved phonon induced electron spin relaxation times at low temperatures.

Furthermore, sub-surface donors provide bound triplet states for electron spin initialization and read-out via spin-to-charge conversion, in donor-based singlet-triplet qubit and exchange qubit devices. Transport spectroscopy measurements of silicon FinFETs have shown bound two electron excited states of single negative donors in the vicinity of a gate [65]. An interface in the vicinity of donors also suppresses the large oscillations in exchange with donor separation, predicted for deeper and bulk-like donors [92]. This ensures that a qubit operation, based on exchange interaction, makes the qubit more robust against the variations in donor positions. Moreover, for the singlet-triplet qubit, a difference in the depth of the two donors induces the necessary transverse fields, eliminating the need for an external micromagnet or non-zero spin nuclei. These transverse fields, arising from the electron g-factor, can be turned *off* with the same gate bias that couples the electron spins through exchange [93]. This offers an additional advantage in mitigating the undesired dephasing effects from inhomogeneous fields.

A schematic of the singlet-triplet and exchange-only qubit architectures based on donors in silicon is as presented in Fig. 5.1(a) and Fig. 5.1(b) respectively. Two electron spins bound to two sub-surface phosphorous donors in silicon located at different depths define a donor-based singlet-triplet qubit. The difference in depth of the two donors provides the necessary difference in Zeeman splitting of the two donors for an X-rotation of the qubit and can arise from the natural straggle in donor positions from ion-implantation or can be intentionally engineered using STM lithography techniques [27, 94]. A donor-based exchange-only qubit consists of three

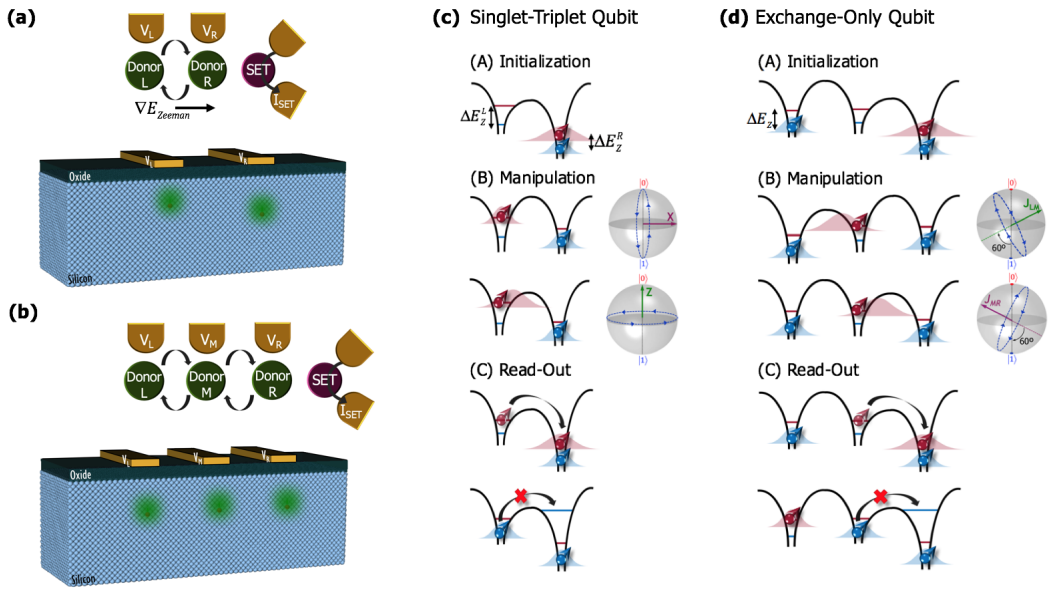

Fig. 5.1. Schematic of sub-surface donor-based singlet-triplet qubit and exchange-only qubit and their operation. **(a)** Singlet-triplet qubit. Two electron spins are bound to two phosphorous atoms (L,R) in silicon at different depths from the oxide-semiconductor interface. The splitting between up and down states ΔE in the two donors comes from dependence of g-factor on the depth of the donor and applied electric field. **(b)** Exchange-only qubit. Three electron spins are bound to three phosphorous donors (L,M,R) in silicon. **(c)** Singlet-Triplet qubit operation. Qubit is initialized to a singlet state in the right donor. Qubit rotations about X and Z axes are achieved when the electrons are isolated and exchange coupled respectively. Qubit state is read-out, by charge sensing the right dot via a nearby single electron transistor SET, at large detuning where singlet state attains a (0,2) charge configuration but a triplet remains blocked in a (1,1) configuration. **(d)** Exchange-only qubit operation. Qubit initialization at a large detuning of right donor to a singlet state. Electrical pulses couple electron spins in left and middle (middle and right) donors for qubit rotations about J_{LM} (J_{MR}) axis. At large detuning of the right donor, a nearby SET charge senses the donor for qubit state measurement. Qubit read-out similar to singlet-triplet qubit where singlet acquires a (1,0,2) charge configuration while triplet is blocked in (1,1,1) configuration.

electron spins bound to three sub-surface phosphorous donors. Fig. 5.1(c) and Fig. 5.1(d) schematically describe the initialization, manipulation and read-out operations

of both qubit architectures proposed. Both qubits are initialized, at a large detuning, to a singlet state with two electrons loaded on one of the donors. Two axis qubit rotations are achieved by electrically tuning exchange in a regime where each donor binds one electron. In a singlet-triplet qubit, turning exchange *on* couples the spins of the two electrons causing qubit rotation about the Z axis on the Bloch sphere. Electron spins are isolated when exchange is turned *off* leading to an X rotation of the two-spin qubit. For a three-spin exchange-only qubit, exchange interaction between two different pairs of electrons is turned *on* to rotate the qubit about two different axes on the Bloch sphere as shown in Fig. 5.1(d). Qubit measurement in both architectures depends on projection of the qubit spin state to a charge state at very large detuning. While the qubit singlet state projects to a charge state with two electrons on a single donor, the triplet state projects to a charge state with one electron on each donor.

Device designs for singlet-triplet and exchange-only qubit based on sub-surface phosphorous donors in silicon are modeled, in this work, with Atomistic configuration interaction ACI, an atomistic many-body approach based on combination of Slater-Koster tight-binding and full configuration interaction, FCI. Atomistic tight-binding models single-electron wavefunctions in realistic, multi-million atom devices, taking into account the atomistic effects of interfaces, defects and complex geometries. Slater determinants constructed from the single-electron states are used as basis in ACI, to solve for the few-electron states. FCI accurately captures Coulomb repulsions between electrons, exchange interactions and correlations and is therefore exact in the space spanned by the select single-electron basis. ACI therefore provides an accurate description of the energy spectra and the spin configurations of the qubit states in the few-electron regime.

5.1 Singlet-Triplet qubit

Two electron spins bound to two donor atoms comprise four lowest energy spin configurations, $|\uparrow_L\uparrow_R\rangle$, $|\uparrow_L\downarrow_R\rangle$, $|\downarrow_L\uparrow_R\rangle$ and $|\downarrow_L\downarrow_R\rangle$. The arrows indicate electron spin orientation and the subscripts indicate localization of electron to the left (L) or right (R) donor. If the electron spins are non-interacting, the two states in the spin-zero subspace $|\uparrow_L\downarrow_R\rangle$ and $|\downarrow_L\uparrow_R\rangle$ remain uncoupled as shown in Fig. 5.2(b). A finite tunnel coupling between the two donors mixes the two states into a spin-anti-symmetric singlet $|S\rangle = |\uparrow_L\downarrow_R - \downarrow_L\uparrow_R\rangle$ and a spin-symmetric triplet $|T_0\rangle = |\uparrow_L\downarrow_R + \downarrow_L\uparrow_R\rangle$ state. The singlet-triplet splitting, or exchange, depends on the exchange interaction between the two electron spins and is modulated electrically by tuning the tunnel coupling between donors. The spin-singlet and spin-triplet states, in the spin-zero subspace, logically define the qubit space of the aptly named singlet-triplet qubit.

Qubit states $|S\rangle$ and $|T_0\rangle$ are represented on a Bloch sphere in Fig. 5.2(c) along the Z-axis. Splitting between the states, exchange J, drives qubit rotations about $J-$axis. Orthogonal states on the X-axis are a linear symmetric $|S\rangle + |T_0\rangle$ and anti-symmetric $|S\rangle - |T_0\rangle$ combination of the qubit states resulting in $|\downarrow_L\uparrow_R\rangle$ and $|\uparrow_L\downarrow_R\rangle$. When exchange is turned *off*, the splitting between the states h triggers a difference in phase evolution of the two uncoupled electron spins which constitutes the X-rotation of the qubit.

Splitting h is the difference in Zeeman splitting of electrons at the two donors due to dissimilar local environments arising either from a gradient magnetic field ΔB or a difference in electron g-factor. The g-factor of an electron bound to a donor depends on the depth of the donor from the Si-SiO_2 interface. By intentionally positioning the donors at different depths or utilizing the naturally occurring vertical straggle in donor implantation, a tunable difference in Zeeman splitting of the two donors can be achieved. Fig. 5.2(a) shows the Zeeman splitting for a single phosphorous donor for varying depths and gate biases at a static magnetic field of 1T. A donor pair high-

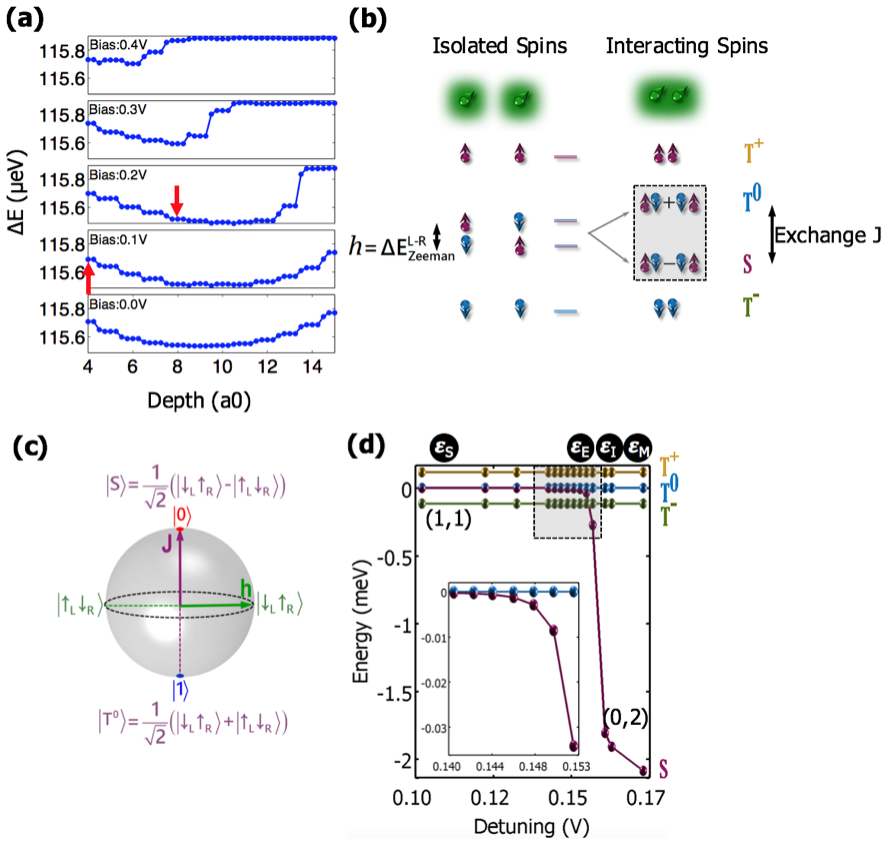

Fig. 5.2. **(a)** Energy splitting ΔE between up and down spins in a donor-dot at 1T static magnetic field with varying donor depths and gate biases. A donor pair with $\Delta E_L - \Delta E_R$ of 0.3μeV, pointed to by red arrows, is randomly selected for demonstrating the singlet-triplet qubit operation using ACI. **(b)** Two-electron spin interactions. For isolated electron spins, the eigenstates $|\uparrow_L\downarrow_R\rangle$ and $|\downarrow_L\uparrow_R\rangle$ are split by the difference in Zeeman splitting between the two donors. A finite tunnel coupling allows the two spins to interact leading to a low-energy spin antisymmetric singlet and a high-energy spin symmetric triplet, split by exchange. Chosen qubit states are highlighted.**(c)** Qubit states $|S\rangle$ and $|T^0\rangle$ represented on the Bloch sphere. Z-gate rotations about axis J in purple are driven by exchange. X-gate rotations about axis h in green are achieved with the difference in ΔE between the donors L and R, when exchange is off. Single qubit operations are implemented with Larmor process using pulse-gating. **(d)** Two-electron energy spectrum for the selected donor pair. (1,1) charge regime for qubit manipulation and (0,2) charge regime for initialization and read-out are accessible. Increasing magnitudes of B separate the $|T^+\rangle$ and $|T^-\rangle$ states from the qubit states. Inset shows qubit states $|S\rangle$ and $|T^0\rangle$ in the (1,1) qubit manipulation regime. Splitting between qubit states estimates X-gate rotations upto 60MHz at small detuning and Z-gate rotations upto 2GHz at positive detuning.

lighted with *red* arrows is randomly chosen to demonstrate the operation of a singlet-triplet qubit. The selected pair has a difference in Zeeman splitting of 0.3μeV corresponding to an equivalent magnetic field gradient of 2.6mT.

A device schematic of the singet-triplet qubit is as shown in Fig. 5.1(a) with two donors at depths $d_L = 4a_0$ and $d_R = 8a_0$ from silicon-oxide interface and separated by r=15nm along [100] crystal direction. An electrical qubit control is achieved by detuning the donors with top gate biases V_L and V_R. Here, detuning lowers the potential of the right donor R relative to the left donor L, $\epsilon = V_L - V_R$ while V_L is held constant. Fig. 5.2(d) describes the evolution of eigenstates of the system with varying detuning for the singlet-triplet qubit. At small detuning ϵ_S, the electron spins are uncoupled and the eigenstates of the transverse fields are split by h. At moderate detuning ϵ_E, tunnel coupling between the donors increases the mixing of two electron spins which lowers the energy of the singlet state relative to the spin-zero triplet by exchange J. The non-zero spin triplets are separated from the spin-zero triplet by Zeeman energy, that remains constant with detuning. At much higher detuning ϵ_M, the potential of the donor R is sufficiently low to energetically favor two electrons on the donor R over one electron on each donor.

Qubit is initialized at large detuning ϵ_I to singlet state in (0,2) charge configuration. Detuning is swept rapidly over S-T_- anti-crossing (shown in Fig. 5.2(d) as a crossing, in the absence of hyperfine fields) and then adiabatically to ϵ_S in (1,1) charge regime. Qubit state is held at ϵ_S for singlet separation time τ_S where electron spins are decoupled. τ_S determines singlet-triplet mixing with an X-rotation of the qubit on the Bloch sphere at frequency close to 50MHz corresponding to the splitting between the eigenstates at ϵ_S. Pulsing to ϵ_E for a time τ_E turns exchange *on*. Exchange couples the two electron spins causing a Z-rotation on the Bloch sphere at 2GHz, as extracted from the singlet-triplet splitting at ϵ_E. Qubit state is returned to large detuning at ϵ_M for measurement. Qubit in a singlet state is projected to the singlet state with two electrons on the right donor R and attains a (0,2) charge configuration while the triplet state remains blocked in (1,1) configuration due to large

exchange of a (0,2) triplet. Sensing the charge on right donor R via a nearby single electron transistor SET measures the qubit state.

5.2 Exchange-only qubit

Three electron spins in a single qubit demand complex spin control sequences. But, high-frequency electrical gating offers high speed qubit rotations for a full two-axis control using only electrically manipulated exchange interactions, between two of the three possible pairs of electron spins. Three electron spins confined to three donor atoms (left L, middle M and right R) have eight spin configurations, a spin +3/2 singlet $|\uparrow_L\uparrow_M\uparrow_R\rangle$; spin +1/2 triplets $|\uparrow_L\uparrow_M\downarrow_R\rangle$, $|\uparrow_L\downarrow_M\uparrow_R\rangle$ and $|\downarrow_L\uparrow_M\uparrow_R\rangle$; spin -1/2 triplets $|\uparrow_L\downarrow_M\downarrow_R\rangle$, $|\downarrow_L\uparrow_M\downarrow_R\rangle$ and $|\downarrow_L\downarrow_M\uparrow_R\rangle$ and; a spin -3/2 singlet $|\downarrow_L\downarrow_M\downarrow_R\rangle$. A static magnetic field parts the states with different net spins by the Zeeman energy as shown in Fig. 5.3(a). For isolated electron spins, the triplets in the spin 1/2 basis do not mix.

A non-zero tunnel coupling between the donors couples the three electron spins and the degeneracy of spin 1/2 triplets is lifted with the formation of a lower energy triplet $|D'\rangle = |\downarrow_M\rangle|T^0_{LR}\rangle - 2|\uparrow_M\rangle|T^-_{LR}\rangle$, a singlet $|D\rangle = |\downarrow_M\rangle|S_{LR}\rangle$ and a higher energy triplet $|D'\rangle = |\downarrow_M\rangle|T_{LR}\rangle - 2|\uparrow_M\rangle|T^-_{LR}\rangle$ for the spin -1/2 subspace and correspondingly for the spin +1/2 triplets as well at zero detuning. The electrons in the left and right donors L and R, are far enough to not interact at zero detuning and the degeneracy of the localized electron states in these two donors make the two-electron triplet $|T^0_{LR}\rangle = |\uparrow_L\downarrow_R\rangle + |\downarrow_L\uparrow_R\rangle$ lower in energy than the singlet $|S_{LR}\rangle = |\uparrow_L\downarrow_R\rangle - |\downarrow_L\uparrow_R\rangle$. The two lower energy states $|D'\rangle$ and $|D\rangle$ in the spin -1/2 subspace are an obvious choice for a logical qubit space.

The basis states $|D'\rangle$ and $|D\rangle$ of the three-spin qubit are as represented on Bloch sphere in Fig. 5.3(b). A higher V_R compared to V_L, corresponding to a positive detuning at ϵ_{MR}, detunes the right donor R relative to the middle donor M and couples the electron spins on donors M and R. The eigenstates at ϵ_{MR}, singlet $|D'\rangle =$

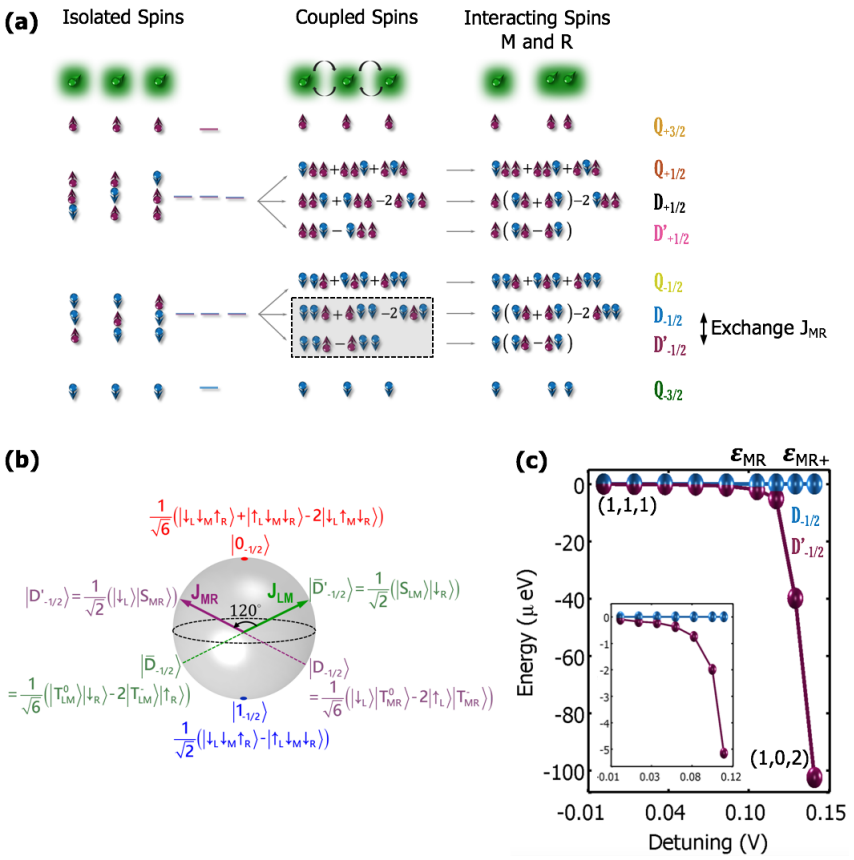

Fig. 5.3. **(a)** Three electron spin interaction. Isolated electron spins are split by Zeeman splitting in a static magnetic field. When the spins are tunnel coupled, the states with same total spin mix with each other and the corresponding eigenstates are as represented. Selected qubit states in the spin -1/2 subspace are highlighted. Two of the three electron spins, middle M and right R spins shown here as an example, interact and form a three-spin singlet and triplet states which are used for qubit rotations. **(b)** Qubit states $|0\rangle$ and $|1\rangle$ in spin -1/2 subspace on the Bloch sphere. At positive detuning ϵ_+ of right donor R, qubit states $|0\rangle$ and $|1\rangle$ couple to the (1,0,2) singlet $|D'\rangle$ and triplet $|D\rangle$ states respectively. Exchange between electrons in donors M and R drives the qubit rotation about axis J_{MR}. Rotation about a second axis J_{LM} achieved with a negative detuning, detuning left donor L, at ϵ_-. Single qubit gate operations accomplished by pulsing to ϵ_+ and ϵ_- **(c)** Energy spectrum of three-electron qubit states for donor separation r=15nm and static magnetic field B=0.1T at positive detuning. (1,1,1) charge regime for qubit manipulations and (1,0,2) charge regime for initialization and read-out are accessible for donors at higher detuning $\epsilon \gg \epsilon_+$. Inset shows the highlighted region with qubit states $|D'\rangle$ and $|D\rangle$ zoomed into (1,1,1) regime. Exchange splitting determines qubit rotations about J_{MR} axis upto 10 GHz.

$|\downarrow_L\rangle |S_{MR}\rangle$ and triplet $|D\rangle = |\downarrow_L\rangle |T^0_{MR}\rangle - 2 |\uparrow_L\rangle \left|T^-_{MR}\right\rangle$, show the exchange interaction between the electrons in donors M and R. States $|D'\rangle$ and $|D\rangle$ at ϵ_{MR} are represented on the Bloch sphere along an axis J_{MR} inclined at 60° to the Z-axis. An exchange pulse at detuning ϵ_{MR} controls the spin interactions of three electrons to drive qubit rotations about the axis J_{MR}. Similarly, a lower V_R compared to V_L, corresponding to a negative detuning at ϵ_{LM}, detunes the left donor L relative to the middle donor M. Pulsing to ϵ_{LM} results in a qubit rotation about the axis J_{LM}, where exchange between electrons on donors L and M splits the singlet $|D'\rangle = |\downarrow_L\rangle |S_{MR}\rangle$ and triplet $|D\rangle = |\downarrow_L\rangle |T^0_{MR}\rangle - 2 |\uparrow_L\rangle \left|T^-_{MR}\right\rangle$ states as shown on Bloch sphere. At higher detuning $\epsilon_{MR+}(\epsilon_{LM-})$, the configurations with two electrons in donor R(L) are preferred over configurations with three electrons in three separate donors.

Device schematic for exchange qubit is as presented in Fig. 5.1(b). Three phoshorous donors at depth d=6a0 are separated by r=15nm along [100] crystal direction. A static magnetic field of 0.1T is assumed. Top gate biases V_L, V_M and V_R dictate electron confinement and only gates V_L and V_R are pulsed to tune the donors relative to each other. Owing to the symmetry of the donor placement here, assumed for simplicity, the energy spectra for positive and negative detuning are expected to be symmetric. In general however, the two detuning regimes are determined by the tunnel coupling between the L-M and M-R donors which modifies the detuning axis and the slopes $dJ/d\epsilon$ of exchange curves. This only requires reevaluating the detuning ϵ_{MR} and ϵ_{LM} for qubit manipulation but does not effect the single qubit operation mechanism significantly. Fig. 5.3(c) shows only the evolution of qubit states corresponding to a varying positive detuning.

A single qubit operation is similar to the exchange qubit operation in gate-defined dots. Qubit state is initialized at large detuning ϵ_I to a singlet state in (1,0,2) charge configuration. Two-axis rotations for qubit manipulation can be achieved via EO, RX or AEON pulsing. As in the EO approach, detuning is swept rapidly over $Q - D'$ anti-crossing in Fig. 5.3(c) (not shown here) and then adiabatically to ϵ_{MR} in (1,1,1) charge regime. System is held at ϵ_{MR} for time τ_{MR} to allow evolution of the qubit

state between singlet $|D'\rangle$ and triplet $|D\rangle$ corresponding to electron spins in middle and right donors. Separation time τ_{MR} determines singlet-triplet mixing causing a rotation of the qubit state about J_{MR}-axis on the Bloch sphere. Rotation frequencies are estimated to be upto 10GHz corresponding to the exchange splitting at ϵ_{MR}. Pulsing to ϵ_{LM}, not shown in the simulation results but symmetrically located along the negative detuning axis, for a time τ_{LM} rotates the qubit about J_{LM}-axis controlled by exchange between electron spins in left and middle donors. Qubit state is returned to large detuning at ϵ_{MR+} for measurement, by charge sensing the right donor R with an SET. Qubit in singlet state $|D'\rangle$ is projected onto the singlet state in right donor in a (1,0,2) charge configuration. Triplet state $|D\rangle$ remains blocked in (1,1,1) charge configuration due to spin blockade.

However, if exchange begins to decrease in the (1,0,2) charge configuration as shown in the Fig. 5.3(c) after ϵ=0.13V, (1,0,2) triplets become energetically accessible and the read-out fidelity deteriorates. This drop in exchange is explained by the two-electron energy spectrum of a single sub-surface donor. At moderate electric fields, the electron wavefunctions hybridize with the interface well states. In this regime, the two electrons are delocalized and spatially separated which decreases the exchange interaction of the electron spins. To ensure a continuously increasing exchange in the (1,0,2) configuration, the donor R must be in an interfacial regime. This two-electron regime occurs at high electric fields where both electrons are localized at the interface well. Increasing the electric field further, increases the confinement of electron wavefunction and thus the exchange interaction of electron spins. Therefore, by modifying the detuning axis as to increase the gate bias, changes the electric field from E=25MV/m to E=30MV/m and places the donor R in the preferred interfacial regime in the (1,0,2) charge configuration. Fig. 5.4(b) shows exchange continues to increase with detuning for larger electric fields.

Qubit states $\left|D'_{-1/2}\right\rangle$ and $\left|D_{-1/2}\right\rangle$ must be isolated from the other six spin configurations to prevent leakage into those states. Increasing the magnitude of the static magnetic field B from 0.1T to 0.5T will increase the splitting between states with

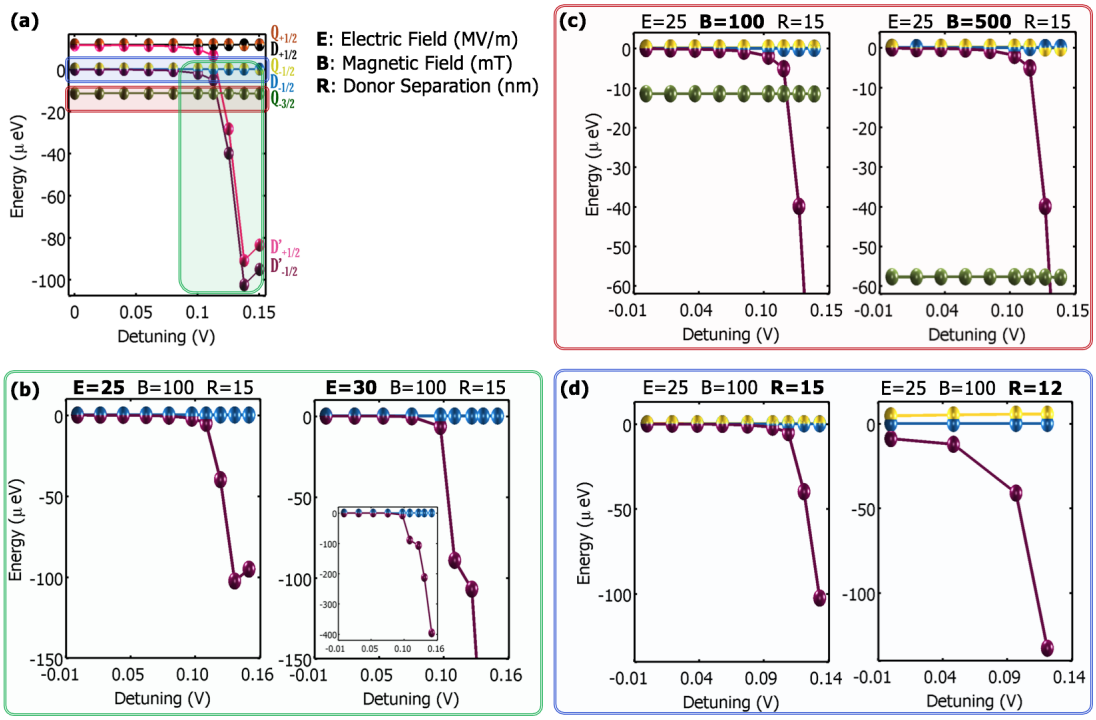

Fig. 5.4. **(a)** Three-electron energy spectrum for donor separation r=15nm and static magnetic field B=0.1T at positive detuning. Highlighted regions show (i) $\left|Q_{-3/2}\right\rangle$ and $\left|D'_{-1/2}\right\rangle$ anti-crossing in the (1,1,1) manipulation regime (ii) $\left|Q_{-1/2}\right\rangle$ leakage state close in energy to qubit states (iii) Increasing energy of $|D'\rangle$ states with increasing detuning in the (1,0,2) charge regime at $\epsilon \geq$0.13V, decreases exchange and thus reduces the read-out fidelity. **(b)** Three-electron energy spectrum for d=15nm and B=0.1T about a detuning axis that ensures a continuing increase in exchange, $|D'\rangle$ and $|D\rangle$ splitting, with detuning in (1,0,2) charge configuration thus ensuring triplet $|D\rangle$ remains blocked in (1,1,1) charge configuration. Inset shows the corresponding highlighted (1,1,1) manipulation regime. **(c)** Three-electron energy spectrum at r=15nm and B=0.5T, isolating spin -1/2 states from spin $\pm$3/2 and spin +1/2 states to prevent leakage from qubit subspace. $\left|Q_{-3/2}\right\rangle$ and $\left|D'_{-1/2}\right\rangle$ cross in the (1,0,2) charge regime. **(d)** Three-electron energy spectrum at B=0.1T for closely spaced donors with r=12nm to separate $\left|Q_{-1/2}\right\rangle$ from qubit states. An increased tunnel coupling between donor-dots increases splitting between $\left|Q_{-1/2}\right\rangle$ and $\left|D_{-1/2}\right\rangle$.

different spin projection on Z. As shown in Fig. 5.4(c), the spin -3/2 and spin +1/2 states are separated by about 50μeV from the spin -1/2 states and the $\left|D'_{-1/2}\right\rangle$ and $\left|Q_{-3/2}\right\rangle$ anti-crossing (shown as crossing here) lies outside the qubit manipulation regime in the (1,1,1) configuration at large B fields. But the $\left|Q_{-1/2}\right\rangle$ still remains a potential leakage state. The splitting between $\left|D_{-1/2}\right\rangle$ and $\left|Q_{-1/2}\right\rangle$ is determined by the tunnel coupling between donors M and R. Decreasing the donor separation from r=15nm to r=12nm increases the tunnel coupling and thus the energy splitting between $\left|D_{-1/2}\right\rangle$ and $\left|Q_{-1/2}\right\rangle$, as seen from Fig. 5.4(d).

5.3 Discussion

Qubits based on donors are robust against variations in donor depth and donor separations. For sub-surface donors, the donor states have a dominant z-valley contribution making exchange relatively less sensitive to the valley interferences arising from varying donor separations in the x-y plane. The oscillations in exchange with separation distance and direction of separation are suppressed for donors close to the interface [92]. For donors located at random depths and separations, a correct detuning axis can be determined from the corresponding charge stability diagram and the gate biases are pulsed accordingly. Alternate device architectures may be more feasible for fabrication like use of a global back gate for exchange qubit: that eliminates the middle gate and allows wider left and right gate geometries.

For both exchange-only and singlet-triplet qubits, the hyperfine fields from donor nuclei, that can potentially couple the qubit states, are suppressed at high magnetic fields and hence ignored. The coupling requires flip-flop processes between the nuclear and bound electron spins which is avoided due to non-availability of phonons, of energy corresponding to the large difference in Zeeman splittings of electron and nuclear spin states, at low temperatures. The electron-electron dipole and nuclear dipole interactions are also disregarded since they decay as r^{-3} and are negligible for the donor separations considered here.

5.4 Summary

Quantum computing devices based on donors in silicon have attracted con- siderable attention towards scalable architectures owing to the consistency of donor atom potentials in an atomically precise array of dopants, deterministically embedded using STM lithography techniques. Donor bound electron spins have been shown to have exceptionally long coherence times, exceeding several seconds at cryogenic temperatures, making the spins of these electrons attractive for quantum information processing. While a single electron spin qubit relies on microwave pulses for qubit rotation, qubits of two and three electron spins achieve rotations by electrically tuning the exchange interactions between electron spins. Coherent, high-frequency gate operations of two and three spin qubits have been demonstrated successfully with electrons confined to electrostatically-defined quantum dots. However, realization of multiple electron spin qubits confined to dopant atoms in silicon has been constrained mainly by (a) loosely confined singlet state and non-availability of bound triplet states, requisite for qubit read-out and; (b) oscillations in exchange with donor separation which necessitates a precise gate control for qubit rotation.

To address these challenges towards realization of donor bound electron spin qubits in silicon, device architectures that confine triplet states and mit- igate the oscillations in exchange are proposed in this work. Two and three spin qubit manipulations depend on electrical tuning of exchange interactions between electrons and an accurate estimation of these interactions is crucial for high fidelity single qubit gate operations. Proposed two-spin singlet-triplet qubit and three-spin exchange-only qubit architectures based on dopants in silicon, that enable an all-electrical qubit control, are studied using ACI.

Two-axis rotations about Z and X axis on the Bloch sphere for the two-spin singlet-triplet qubit are achieved using electrical and depth detuning, respectively. Detuning the potentials of the two donors changes the exchange leading to Z rotation of the qubit. Positioning the donors at different depths changes the g-factor and

thus the difference in Zeeman splitting between the two donor states. This allows an X-rotation of a two-spin qubit without the need for a gradient magnetic field from an integrated micromagnet or non-zero nuclear spins. For three-spin exchange only qubit, rotations about both axis are achieved using exchange between two different pairs of electrons. The qubit states can be isolated from the leakage states by tuning the electric and magnetic fields and the donor separation. The evolution of the two- and three-electron states with detuning is obtained from ACI and an all-electrical two-axis rotations are demonstrated in this work.

6. SUMMARY

A coherent control of a single electron spin qubit in semiconductor devices has been successfully demonstrated, for electrons bound to electrostatic gate-defined quantum dots and dopant atoms. Two-qubit logic gates for electron spin qubits rely on electron-electron interactions, tuanble electrically with gate biases. A precise gate control of a two-qubit operation demands an accurate estimation of the electron interactions, taking into account the atomistic details of the realistic qubit devices.

Atomistic Configuration Interaction (ACI), an atomistic many-body approach based on a combination of Slater-Koster tight-binding and full configuration interaction, is developed and implemented in Nano-Electronic MOdeling (NEMO) simulation software suite to model multi-electron devices on an atomic scale. The code is massively parallelized over several thousands of cores using MPI and OpenMP threads. Shared memory models enable simulation of a system of large number of atoms with a large single-electron basis for a more accurate description of the few-electron states. The most demanding computations in ACI are identified and Fast Multipole Method (FMM) is implemented to reduce the computational complexity in evaluating electron-electron interactions.

ACI method is validated against several few-electron experiments. Two-electron charging and binding energies of a bulk phosphorous donor in silicon match closely with those from optical experiments. Moreover, the configuration of these two-electron states from ACI reveals that the probability of both electrons occupying $1s$ states of the donor D^0 is only 37% while there is a significant 56% probability of the one of the electrons occupying the $2s$ donor D^0 state. STM probing of the two-electron states of a sub-surface arsenic donor and tip-induced quantum dot in a resonant tunneling experiment, by Prof. Rogge's group at CQCCT, shows a good agreement with ACI simulations. The geometry of the set-up, including the

tip and highly doped reservoir, are parameterized against the binding energies of the tip-induced quantum dot. The effect of electrostatics of the device in screening the electron-electron interactions, also implemented in ACI, is found to be significant. In a similar STM experiment, sub-surface phosphorous donors are investigated. ACI modeling of these donors enabled an understanding of the oscillations in exchange with donor separation distance and direction and the correlation between exchange oscillations and valley interferences, by comparing the results against the STM images and spatially resolved differential conductance spectrum of the donor pairs. The addition energies in single-valley GaAs quantum dot agree reasonably well qualitatively with the available experimental data. Smaller, elliptical dots are used in ACI simulations to reduce the computational burden in simulating the GaAs dot loaded with upto 12 electrons. Furthermore, ACI also provides the multi-electron configurations to aide in understanding the shell filling in these GaAs quantum dots.

For further insights into the physics of the multi-electron systems, ACI is used to explore the effect of different environmental and structural parameters on the few-electron spectra. For a sub-surface negative phosphorous donor in silcion, the influence of applied electric field, the depth of the donor and the electrostatics of the interfaces on the two-electron states of the donor are determined. Sub-surface neutral phosphorous donor pairs are also studied with ACI. The invalidity of the approximate methods, like Heitler-London and Hartree-Fock, in evaluating exchange is demonstrated. ACI simulations show that the exchange saturates for closely spaced donors, against the intuitive extrapolation of the exponential increase in exchange with decreasing donor separation. Furthermore, the oscillations in exchange are suppressed as the donors move closer to the silicon surface. However, the charging energy is fairly monotonic with both donor separation and depth. ACI simulations of multi-electron silicon quantum dot show that the

ACI is employed to evaluate the performance of novel qubit devices. Two and three electron spin qubits, based on dopants in silicon, are proposed in this work. All electrical control of these qubits is demonstrated from ACI simulations. The

challenges in realization of multi-spin qubits in donors like the non-availability of bound triplet states on a single donor and the oscillations in exchange with donor separation, are addressed with the use of sub-surface donors. For two-spin singlet-triplet qubit, the qubit rotation along X can be achieved by tuning the relative depths of the donors, without the use of micromagnets or non-zero spin nuclei, for an all-electrical qubit control. In exchange-only qubit, the qubit states are shown to be isolated from the leakage states by tuning the magnetic field, electric field and the donor separation.

In the future, ACI will be used to study the control of a donor-based singlet-triplet qubit using coplanar waveguides, CPW. For donor separations between 4nm to 6nm, the singlet and triplet states have different two-electron orbital wavefunctions, as observed from the two-electron ACI wavefunctions. This causes a large dipole that can potentially be manipulated by superconducting CPW resonators. ACI can also be used to study few-electron hybrid qubits in GaAs or silicon structures, multi-qubit coupling in realistic quantum dot and dopant based devices and in two- and three-electron spin relaxation times. ACI tool implemented in NEMO software suite, thus, enables modeling and engineering multi-electron interactions for quantum logic operations, towards scalable quantum computing devices.

REFERENCES

REFERENCES

[1] C. A. Mack, "Fifty years of moore's law," *IEEE Transactions on semiconductor manufacturing*, vol. 24, no. 2, pp. 202–207, 2011.

[2] M. Bohr, "The evolution of scaling from the homogeneous era to the heterogeneous era," in *Electron Devices Meeting (IEDM), 2011 IEEE International*. IEEE, 2011, pp. 1–1.

[3] A. P. Jacob, R. Xie, M. G. Sung, L. Liebmann, R. T. Lee, and B. Taylor, "Scaling challenges for advanced cmos devices," *International Journal of High Speed Electronics and Systems*, vol. 26, no. 01n02, p. 1740001, 2017.

[4] N. Hemsoth, "Thomas sterling: I think we will never reach zettaflops," 2012, https://www.hpcwire.com/2012/05/07/thomas_sterling_i_think_we_will_never_reach_zettaflops_/.

[5] T. D. Ladd, F. Jelezko, R. Laflamme, Y. Nakamura, C. Monroe, and J. L. O'Brien, "Quantum computers," *Nature*, vol. 464, no. 7285, pp. 45–53, 2010.

[6] P. W. Shor, "Polynomial-time algorithms for prime factorization and discrete logarithms on a quantum computer," *SIAM review*, vol. 41, no. 2, pp. 303–332, 1999.

[7] L. K. Grover, "A fast quantum mechanical algorithm for database search," in *Proceedings of the twenty-eighth annual ACM symposium on Theory of computing*. ACM, 1996, pp. 212–219.

[8] E. Farhi, J. Goldstone, S. Gutmann, J. Lapan, A. Lundgren, and D. Preda, "A quantum adiabatic evolution algorithm applied to random instances of an np-complete problem," *Science*, vol. 292, no. 5516, pp. 472–475, 2001.

[9] H.-A. Bachor and M. Simmons, "Quantum computing," 2017, http://www.nova.org.au/technology-future/quantum-computing.

[10] M. Simmons, "The development of a quantum computer in silicon," 2013, http://www.ieeesisc.org/tutorials/2013_SISC_Tutorial.pdf.

[11] J. J. Pla, K. Y. Tan, J. P. Dehollain, W. H. Lim, J. J. Morton, D. N. Jamieson, A. S. Dzurak, and A. Morello, "A single-atom electron spin qubit in silicon," *Nature*, vol. 489, no. 7417, pp. 541–545, 2012.

[12] F. Koppens, C. Buizert, K.-J. Tielrooij, I. Vink, K. Nowack, T. Meunier, L. Kouwenhoven, and L. Vandersypen, "Driven coherent oscillations of a single electron spin in a quantum dot," *Nature*, vol. 442, no. 7104, pp. 766–771, 2006.

[13] J. Elzerman, R. Hanson, L. W. Van Beveren, B. Witkamp, L. Vandersypen, and L. P. Kouwenhoven, "Single-shot read-out of an individual electron spin in a quantum dot," *nature*, vol. 430, no. 6998, pp. 431–435, 2004.

[14] A. Morello, J. J. Pla, F. A. Zwanenburg, K. W. Chan, K. Y. Tan, H. Huebl, M. Möttönen, C. D. Nugroho, C. Yang, J. A. van Donkelaar *et al.*, "Single-shot readout of an electron spin in silicon," *Nature*, vol. 467, no. 7316, pp. 687–691, 2010.

[15] J. R. Petta, A. C. Johnson, J. M. Taylor, E. A. Laird, A. Yacoby, M. D. Lukin, C. M. Marcus, M. P. Hanson, and A. C. Gossard, "Coherent manipulation of coupled electron spins in semiconductor quantum dots," *Science*, vol. 309, no. 5744, pp. 2180–2184, 2005.

[16] J. M. Nichol, L. A. Orona, S. P. Harvey, S. Fallahi, G. C. Gardner, M. J. Manfra, and A. Yacoby, "High-fidelity entangling gate for double-quantum-dot spin qubits," *arXiv preprint arXiv:1608.04258*, 2016.

[17] M. Veldhorst, J. Hwang, C. Yang, A. Leenstra, B. De Ronde, J. Dehollain, J. Muhonen, F. Hudson, K. M. Itoh, A. Morello *et al.*, "An addressable quantum dot qubit with fault-tolerant control-fidelity," *Nature Nanotechnology*, vol. 9, no. 12, pp. 981–985, 2014.

[18] A. Tyryshkin, S. Lyon, W. Jantsch, and F. Schäffler, "Spin manipulation of free two-dimensional electrons in si/sige quantum wells," *Physical review letters*, vol. 94, no. 12, p. 126802, 2005.

[19] J. J. Pla, K. Y. Tan, J. P. Dehollain, W. H. Lim, J. J. Morton, F. A. Zwanenburg, D. N. Jamieson, A. S. Dzurak, and A. Morello, "High-fidelity readout and control of a nuclear spin qubit in silicon," *Nature*, vol. 496, no. 7445, pp. 334–338, 2013.

[20] S. Schofield, N. Curson, M. Simmons, F. Rueß, T. Hallam, L. Oberbeck, and R. Clark, "Atomically precise placement of single dopants in si," *Physical Review Letters*, vol. 91, no. 13, p. 136104, 2003.

[21] A. Tyryshkin, S. Lyon, A. Astashkin, and A. Raitsimring, "Electron spin relaxation times of phosphorus donors in silicon," *Physical Review B*, vol. 68, no. 19, p. 193207, 2003.

[22] G. Klimeck, "Nemo5, a parallel, multiscale, multiphysics nanoelectronics modeling tool," 2016.

[23] I. NEMO, "Multimillion atom simulations with nemo 3-d."

[24] R. Ferdous, E. Kawakami, P. Scarlino, M. P. Nowak, D. Ward, D. Savage, M. Lagally, S. Coppersmith, M. Friesen, M. A. Eriksson *et al.*, "Valley dependent anisotropic spin splitting in silicon quantum dots," *arXiv preprint arXiv:1702.06210*, 2017.

[25] A. Baldereschi, "Valley-orbit interaction in semiconductors," *Physical Review B*, vol. 1, no. 12, p. 4673, 1970.

[26] G. Klimeck, S. S. Ahmed, H. Bae, N. Kharche, S. Clark, B. Haley, S. Lee, M. Naumov, H. Ryu, F. Saied *et al.*, "Atomistic simulation of realistically sized nanodevices using nemo 3-dpart i: Models and benchmarks," *IEEE Transactions on Electron Devices*, vol. 54, no. 9, pp. 2079–2089, 2007.

[27] M. Fuechsle, J. A. Miwa, S. Mahapatra, H. Ryu, S. Lee, O. Warschkow, L. C. Hollenberg, G. Klimeck, and M. Y. Simmons, "A single-atom transistor," *Nature Nanotechnology*, vol. 7, no. 4, pp. 242–246, 2012.

[28] B. Weber, S. Mahapatra, H. Ryu, S. Lee, A. Fuhrer, T. Reusch, D. Thompson, W. Lee, G. Klimeck, L. C. Hollenberg *et al.*, "Ohms law survives to the atomic scale," *Science*, vol. 335, no. 6064, pp. 64–67, 2012.

[29] D. P. DiVincenzo, D. Bacon, J. Kempe, G. Burkard, and K. B. Whaley, "Universal quantum computation with the exchange interaction," *Nature*, vol. 408, no. 6810, pp. 339–342, 2000.

[30] L. Gaudreau, S. Studenikin, A. Sachrajda, P. Zawadzki, A. Kam, J. Lapointe, M. Korkusinski, and P. Hawrylak, "Stability diagram of a few-electron triple dot," *Physical review letters*, vol. 97, no. 3, p. 036807, 2006.

[31] á. Gaudreau, G. Granger, A. Kam, G. Aers, S. Studenikin, P. Zawadzki, M. Pioro-Ladriere, Z. Wasilewski, and A. Sachrajda, "Coherent control of three-spin states in a triple quantum dot," *Nature Physics*, vol. 8, no. 1, pp. 54–58, 2012.

[32] J. Medford, J. Beil, J. Taylor, E. Rashba, H. Lu, A. Gossard, and C. M. Marcus, "Quantum-dot-based resonant exchange qubit," *Physical review letters*, vol. 111, no. 5, p. 050501, 2013.

[33] J. Taylor, V. Srinivasa, and J. Medford, "Electrically protected resonant exchange qubits in triple quantum dots," *Physical review letters*, vol. 111, no. 5, p. 050502, 2013.

[34] A. Szabo and N. S. Ostlund, *Modern quantum chemistry: introduction to advanced electronic structure theory*. Courier Corporation, 2012.

[35] W. A. Harrison, *Electronic structure and the properties of solids: the physics of the chemical bond*. Courier Dover Publications, 2012.

[36] J. Slater and G. Koster, "Wave functions for impurity levels," *Phy. Rev*, vol. 94, p. 1498, 1954.

[37] R. Rahman, L. C. Hollenberg, and G. Klimeckc, "Theory and simulations of controlled electronic states bound to a single dopant in silicon," *Single-Atom Nanoelectronics*, p. 41, 2016.

[38] R. Rahman, G. P. Lansbergen, S. H. Park, J. Verduijn, G. Klimeck, S. Rogge, and L. C. L. Hollenberg, "Orbital stark effect and quantum confinement transition of donors in silicon," *Physical Review B*, vol. 80, no. 16, p. 165314, 2009.

[39] S. H. Park, "Hyperfine mapping of donor wave function deformations in silicon phosphorus based quantum devices," Ph.D. dissertation, Purdue University, 2009.

[40] M. Naumov, S. Lee, B. Haley, H. Bae, S. Clark, R. Rahman, H. Ryu, F. Saied, and G. Klimeck, "Eigenvalue solvers for atomistic simulations of electronic structures with nemo-3d," *Journal of Computational Electronics*, vol. 7, no. 3, pp. 297–300, 2008.

[41] R. Rahman, E. Nielsen, R. P. Muller, and M. S. Carroll, "Voltage controlled exchange energies of a two-electron silicon double quantum dot with and without charge defects in the dielectric," *Physical Review B*, vol. 85, no. 12, p. 125423, 2012.

[42] H. Sahasrabudhe, B. Novakovic, J. Nakamura, S. Fallahi, M. Povolotskyi, G. Klimeck, R. Rahman, and M. J. Manfra, "Optimization of edge state velocity in the integer quantum hall regime," *arXiv preprint arXiv:1705.07005*, 2017.

[43] M. Galgon, L. Krämer, and B. Lang, "The feast algorithm for large eigenvalue problems," *PAMM*, vol. 11, no. 1, pp. 747–748, 2011.

[44] E. Anderson, Z. Bai, J. Dongarra, A. Greenbaum, A. McKenney, J. Du Croz, S. Hammerling, J. Demmel, C. Bischof, and D. Sorensen, "Lapack: A portable linear algebra library for high-performance computers," in *Proceedings of the 1990 ACM/IEEE conference on Supercomputing*. IEEE Computer Society Press, 1990, pp. 2–11.

[45] T. Takashima and R. Ishibashi, "Electric fields in dielectric multi-layers calculated by digital computer," *IEEE Transactions on Electrical Insulation*, no. 1, pp. 37–44, 1978.

[46] R. Yokota and L. A. Barba, "Treecode and fast multipole method for N-body simulation with CUDA," *GPU Computing Gems Emerald Edition*, pp. 113–132, 2011.

[47] R. Duraiswami and N. A. Gumerov, "Fast multipole methods: Fundamentals and applications," 2002, http://www.umiacs.umd.edu/~ramani/cmsc878R/Lecture1_Introduction_06.pdf.

[48] R. Yokota, "12 steps to a fast multipole method," 2011, https://www.bu.edu/pasi/files/2011/01/RioYokota1-06-0900.pdf.

[49] Y. Wang, A. Tankasala, L. C. Hollenberg, G. Klimeck, M. Y. Simmons, and R. Rahman, "Highly tunable exchange in donor qubits in silicon," *NPJ Quantum Information*, vol. 2, p. 16008, 2016.

[50] Y. Hsueh, A. Tankasala, Y. Wang, G. Klimeck, M. Simmons, and R. Rahman, "Phonon induced two-electron relaxation in two donor qubits in silicon," in *APS March Meeting Abstracts*, 2016.

[51] B. E. Kane, "A silicon-based nuclear spin quantum computer," *Nature*, vol. 393, no. 6681, pp. 133–137, 1998.

[52] S.-i. Narita, T. Shinbashi, and M. Kobayashi, "Uniaxial stress and magnetic field effects on far-infrared photoconductivity of d-centers in p, as and li doped si crystals," *Journal of the Physical Society of Japan*, vol. 51, no. 7, pp. 2186–2193, 1982.

[53] M. J. Calderón, J. Verduijn, G. P. Lansbergen, G. C. Tettamanzi, S. Rogge, and B. Koiller, "Heterointerface effects on the charging energy of the shallow D- ground state in silicon: Role of dielectric mismatch," *Physical Review B*, vol. 82, no. 7, p. 075317, 2010.

[54] A. Saraiva, A. Baena, M. Calderón, and B. Koiller, "Theory of one and two donors in silicon," *arXiv preprint arXiv:1407.8224*, 2014.

[55] S. Ahmed, N. Kharche, R. Rahman, M. Usman, S. Lee, H. Ryu, H. Bae, S. Clark, B. Haley, M. Naumov *et al.*, "Multimillion atom simulations with nemo3d," in *Encyclopedia of Complexity and Systems Science*. Springer, 2009, pp. 5745–5783.

[56] M. Taniguchi and S. Narita, "D- state in silicon," *Solid State Communications*, vol. 20, no. 2, pp. 131–133, 1976.

[57] T. B. Boykin, G. Klimeck, and F. Oyafuso, "Valence band effective-mass expressions in the sp3d5s* empirical tight-binding model applied to a Si and Ge parametrization," *Physical Review B*, vol. 69, no. 11, p. 115201, 2004.

[58] V. Srinivasa, H. Xu, and J. M. Taylor, "Tunable spin-qubit coupling mediated by a multielectron quantum dot," *Physical review letters*, vol. 114, no. 22, p. 226803, 2015.

[59] P. R. Cullis and J. Marko, "Determination of the donor pair exchange energy in phosphorus-doped silicon," *Physical Review B*, vol. 1, no. 2, p. 632, 1970.

[60] B. Koiller, X. Hu, and S. D. Sarma, "Exchange in silicon-based quantum computer architecture," *Physical review letters*, vol. 88, no. 2, p. 027903, 2001.

[61] J. Salfi, B. Voisin, A. Tankasala, J. Bocquel, M. Usman, M. Simmons, L. Hollenberg, R. Rahman, and S. Rogge, "Atomically precise control of a coupled donor-quantum dot system in silicon," *Bulletin of the American Physical Society*, vol. 62, 2017.

[62] M. Usman, J. Bocquel, J. Salfi, B. Voisin, A. Tankasala, R. Rahman, M. Y. Simmons, S. Rogge, and L. Hollenberg, "Spatial metrology of dopants in silicon with exact lattice site precision," *Nature nanotechnology*, vol. 11, no. 9, pp. 763–768, 2016.

[63] J. e. a. Bocquel, "Quantum interferences in two exchange coupled dopant atoms," *In preparation*, 2017.

[64] S. Tarucha, D. Austing, T. Honda, R. Van der Hage, and L. P. Kouwenhoven, "Shell filling and spin effects in a few electron quantum dot," *Physical Review Letters*, vol. 77, no. 17, p. 3613, 1996.

[65] G. P. Lansbergen, R. Rahman, J. Verduijn, G. C. Tettamanzi, N. Collaert, S. Biesemans, G. Klimeck, L. C. L. Hollenberg, and S. Rogge, "Lifetime-enhanced transport in silicon due to spin and valley blockade," *Physical Review Letters*, vol. 107, no. 13, p. 136602, 2011.

[66] T. F. Watson, B. Weber, M. G. House, H. Büch, and M. Y. Simmons, "High-fidelity rapid initialization and read-out of an electron spin via the single donor D- charge state," *Physical Review Letters*, vol. 115, no. 16, p. 166806, 2015.

[67] C. D. Hill, E. Peretz, S. J. Hile, M. G. House, M. Fuechsle, S. Rogge, M. Y. Simmons, and L. C. Hollenberg, "A surface code quantum computer in silicon," *Science advances*, vol. 1, no. 9, p. e1500707, 2015.

[68] M. J. Calderon, B. Koiller, X. Hu, and S. DasSarma, "Quantum control of donor electrons at the Si-SiO2 interface," *Physical Review Letters*, vol. 96, no. 9, p. 096802, 2006.

[69] R. Rahman, G. P. Lansbergen, J. Verduijn, G. C. Tettamanzi, S. H. Park, N. Collaert, S. Biesemans, G. Klimeck, L. C. L. Hollenberg, and S. Rogge, "Electric field reduced charging energies and two-electron bound excited states of single donors in silicon," *Physical Review B*, vol. 84, no. 11, p. 115428, 2011.

[70] M. J. Calderón, A. Saraiva, B. Koiller, and S. Das Sarma, "Quantum control and manipulation of donor electrons in Si-based quantum computing," *Journal of Applied Physics*, vol. 105, no. 12, p. 122410, 2009.

[71] G. Pica, B. W. Lovett, R. N. Bhatt, T. Schenkel, and S. A. Lyon, "Surface code architecture for donors and dots in silicon with imprecise and nonuniform qubit couplings," *Physical Review B*, vol. 93, no. 3, p. 035306, 2016.

[72] P. Harvey-Collard, N. T. Jacobson, M. Rudolph, J. Dominguez, G. A. T. Eyck, J. R. Wendt, T. Pluym, J. K. Gamble, M. P. Lilly, M. Pioro-Ladrière *et al.*, "Nuclear-driven electron spin rotations in a single donor coupled to a silicon quantum dot," *arXiv preprint arXiv:1512.01606*, 2015.

[73] B. Voisin, J. Salfi, J. Bocquel, R. Rahman, and S. Rogge, "Spatially resolved resonant tunneling on single atoms in silicon," *Journal of Physics: Condensed Matter*, vol. 27, no. 15, p. 154203, 2015.

[74] B. Voisin, M. Cobian, X. Jehl, M. Vinet, Y.-M. Niquet, C. Delerue, S. de-Franceschi, and M. Sanquer, "Control of the ionization state of three single donor atoms in silicon," *Physical Review B*, vol. 89, no. 16, p. 161404, 2014.

[75] B. Koiller, R. Capaz, X. Hu, and S. D. Sarma, "Shallow-donor wave functions and donor-pair exchange in silicon: Ab initio theory and floating-phase heitler-london approach," *Physical Review B*, vol. 70, no. 11, p. 115207, 2004.

[76] G. Pica, B. W. Lovett, R. Bhatt, and S. Lyon, "Exchange coupling between silicon donors: The crucial role of the central cell and mass anisotropy," *Physical Review B*, vol. 89, no. 23, p. 235306, 2014.

[77] X. Wu, D. R. Ward, J. Prance, D. Kim, J. K. Gamble, R. Mohr, Z. Shi, D. Savage, M. Lagally, M. Friesen *et al.*, "Two-axis control of a singlet–triplet qubit with an integrated micromagnet," *Proceedings of the National Academy of Sciences*, vol. 111, no. 33, pp. 11 938–11 942, 2014.

[78] Y.-P. Shim and C. Tahan, "Charge-noise-insensitive gate operations for always-on, exchange-only qubits," *Physical Review B*, vol. 93, no. 12, p. 121410, 2016.

[79] B. M. Maune, M. G. Borselli, B. Huang, T. D. Ladd, P. W. Deelman, K. S. Holabird, A. A. Kiselev, I. Alvarado-Rodriguez, R. S. Ross, A. E. Schmitz *et al.*, "Coherent singlet-triplet oscillations in a silicon-based double quantum dot," *Nature*, vol. 481, no. 7381, pp. 344–347, 2012.

[80] S. Foletti, H. Bluhm, D. Mahalu, V. Umansky, and A. Yacoby, "Universal quantum control of two-electron spin quantum bits using dynamic nuclear polarization," *Nature Physics*, vol. 5, no. 12, pp. 903–908, 2009.

[81] C. Barthel, D. Reilly, C. M. Marcus, M. Hanson, and A. Gossard, "Rapid single-shot measurement of a singlet-triplet qubit," *Physical Review Letters*, vol. 103, no. 16, p. 160503, 2009.

[82] C. Barthel, J. Medford, C. Marcus, M. Hanson, and A. Gossard, "Interlaced dynamical decoupling and coherent operation of a singlet-triplet qubit," *Physical review letters*, vol. 105, no. 26, p. 266808, 2010.

[83] D. Culcer, Ł. Cywiński, Q. Li, X. Hu, and S. D. Sarma, "Realizing singlet-triplet qubits in multivalley si quantum dots," *Physical Review B*, vol. 80, no. 20, p. 205302, 2009.

[84] J. Klinovaja, D. Stepanenko, B. I. Halperin, and D. Loss, "Exchange-based cnot gates for singlet-triplet qubits with spin-orbit interaction," *Physical Review B*, vol. 86, no. 8, p. 085423, 2012.

[85] C. H. Wong, M. Eriksson, S. Coppersmith, and M. Friesen, "High-fidelity singlet-triplet s- t- qubits in inhomogeneous magnetic fields," *Physical Review B*, vol. 92, no. 4, p. 045403, 2015.

[86] J. Taylor, H.-A. Engel, W. Dür, A. Yacoby, C. Marcus, P. Zoller, and M. Lukin, "Fault-tolerant architecture for quantum computation using electrically controlled semiconductor spins," *Nature Physics*, vol. 1, no. 3, pp. 177–183, 2005.

[87] M. D. Shulman, O. E. Dial, S. P. Harvey, H. Bluhm, V. Umansky, and A. Yacoby, "Demonstration of entanglement of electrostatically coupled singlet-triplet qubits," *Science*, vol. 336, no. 6078, pp. 202–205, 2012.

[88] E. A. Laird, J. M. Taylor, D. P. DiVincenzo, C. M. Marcus, M. P. Hanson, and A. C. Gossard, "Coherent spin manipulation in an exchange-only qubit," *Physical Review B*, vol. 82, no. 7, p. 075403, 2010.

[89] J. Medford, J. Beil, J. Taylor, S. Bartlett, A. Doherty, E. Rashba, D. DiVincenzo, H. Lu, A. Gossard, and C. M. Marcus, "Self-consistent measurement and state tomography of an exchange-only spin qubit," *Nature nanotechnology*, vol. 8, no. 9, pp. 654–659, 2013.

[90] C. Wellard and L. Hollenberg, "Donor electron wave functions for phosphorus in silicon: Beyond effective-mass theory," *Physical Review B*, vol. 72, no. 8, p. 085202, 2005.

[91] B. Koiller, X. Hu, and S. D. Sarma, "Strain effects on silicon donor exchange: Quantum computer architecture considerations," *Physical Review B*, vol. 66, no. 11, p. 115201, 2002.

[92] A. Tankasala, Y. Wang, G. Klimeck, and R. Rahman, "Atomistic configuration interaction simulations of two-electron states of donors in silicon," in *APS Meeting Abstracts*, vol. 1, 2015, p. 37011.

[93] R. Rahman, S. H. Park, T. B. Boykin, G. Klimeck, S. Rogge, and L. C. Hollenberg, "Gate-induced g-factor control and dimensional transition for donors in multivalley semiconductors," *Physical Review B*, vol. 80, no. 15, p. 155301, 2009.

[94] F. J. Ruess, L. Oberbeck, M. Y. Simmons, K. E. J. Goh, A. R. Hamilton, T. Hallam, S. R. Schofield, N. J. Curson, and R. G. Clark, "Toward atomic-scale device fabrication in silicon using scanning probe microscopy," *Nano Letters*, vol. 4, no. 10, pp. 1969–1973, 2004.